bioRxiv preprint doi: https://doi.org/10.1101/2023.05.07.539748; this version posted May 8, 2023. The copyright holder for this preprint (which was not certified by peer review) is the author/funder, who has granted bioRxiv a license to display the preprint in perpetuity. It is made available under aCC-BY-NC-ND 4.0 International license.

DNA repair and anti-cancer mechanisms in the longest-living mammal: the bowhead whale

Denis Firsanov[1]*, Max Zacher[1]*, Xiao Tian[1], Yang Zhao[1], John C. George[2], Todd L. Sformo[2,3], Greg Tombline[1], Seyed Ali Biashad[1], Abbey Gilman[1], Nicholas Hamilton[1], Avnee Patel[1], Maggie Straight[1], Minseon Lee[1], J. Yuyang Lu[1], Ena Haseljic[1], Alyssa Williams[1], Nalani Miller[1], Vadim N. Gladyshev[4], Zhengdong Zhang[5], Jan Vijg[5,#], Andrei Seluanov[1,6,#], Vera Gorbunova[1,6,#]

[1]Department of Biology, University of Rochester, Rochester, NY, USA.
[2]Department of Wildlife Management, North Slope Borough, Utqiaġvik (Barrow), AK 99723, USA
[3]Institute of Arctic Biology, University of Alaska Fairbanks, Fairbanks, AK 99775, USA
[4]Division of Genetics, Department of Medicine, Brigham and Women's Hospital, Harvard Medical School, Boston, MA 02115, USA
[5]Department of Genetics, Albert Einstein College of Medicine, Bronx, NY 10461, USA
[6]Department of Medicine, University of Rochester Medical Center, Rochester, NY, USA
*These authors contributed equally to this work.

[#]Corresponding authors:
Vera Gorbunova
University of Rochester
Email: vera.gorbunova@rochester.edu

Andrei Seluanov
University of Rochester
Email: andrei.seluanov@rochester.edu

Jan Vijg
Albert Einstein College of Medicine
Email: jan.vijg@einsteinmed.edu

bioRxiv preprint doi: https://doi.org/10.1101/2023.05.07.539748; this version posted May 8, 2023. The copyright holder for this preprint (which was not certified by peer review) is the author/funder, who has granted bioRxiv a license to display the preprint in perpetuity. It is made available under aCC-BY-NC-ND 4.0 International license.

Abstract

At over 200 years, the maximum lifespan of the bowhead whale exceeds that of all other mammals. The bowhead is also the second-largest animal on Earth, reaching over 80,000 kg[1]. In spite of its very large number of cells, the bowhead is not highly cancer-prone, an incongruity termed Peto's Paradox[2]. This has been explained by the evolution of additional tumor suppressor genes in larger animals, which is supported by research on elephants demonstrating expansion of the p53 gene[3–5]. However, we show here that bowhead whale fibroblasts undergo oncogenic transformation after disruption of fewer tumor suppressors than required for human fibroblasts. Instead, analysis of DNA repair revealed that bowhead cells repair double-strand breaks with uniquely high efficiency and accuracy compared to other mammals. Further, we identified two proteins, CIRBP and RPA2, that are present at high levels in bowhead fibroblasts and increase the efficiency and fidelity of DNA repair in human cells. These results suggest that rather than possessing additional tumor suppressor genes as barriers to oncogenesis, the bowhead whale relies on more accurate and efficient DNA repair to preserve genome integrity. This strategy that does not eliminate cells but repairs them, may be critical for the long and cancer-free lifespan of the bowhead whale. Our work demonstrates the value of studying long-lived organisms in identifying novel longevity mechanisms and their potential for translation to humans.

Introduction

The Alaskan Iñupiat Inuit, who carry on a long tradition of subsistence hunting of the bowhead whale (*Balaena mysticetus*), maintain that these animals "live two human lifetimes"[6]. Remarkably, a series of bowhead whales captured in the late-twentieth and early-twenty-first centuries lent new credence to these claims, as embedded in their bodies were traditional stone harpoon points and bomb lance fragments dating to the Victorian era[7]. Subsequent scientific study and age estimation through quantification of

bioRxiv preprint doi: https://doi.org/10.1101/2023.05.07.539748; this version posted May 8, 2023. The copyright holder for this preprint (which was not certified by peer review) is the author/funder, who has granted bioRxiv a license to display the preprint in perpetuity. It is made available under aCC-BY-NC-ND 4.0 International license.

ovarian corpora, baleen dating, and eye lens aspartic acid racemization analysis supported a maximum lifespan exceeding 200 years in the bowhead whale[7–12]. Thus, the range of mammalian lifespans covers roughly 2 orders of magnitude, with the model organism *Mus musculus* living for 2-3 years while the bowhead whale lives 100 times as long.

An increased number of cells and cell divisions in larger organisms might be expected to contribute to increased cancer incidence and shorter lifespans. The apparent contradiction between expected and observed cancer rates in relation to species body mass has been noted for decades and is known as Peto's Paradox.[2,13–15] It is theorized to result from compensatory evolutionary adaptations driven by reduced extrinsic mortality in larger species[2]. The bowhead whale exceeds 80,000 kg in mass and 200 years in lifespan. Both of these factors predispose it to accumulating large numbers of DNA mutations throughout life. To remain alive for so long it must possess uniquely potent genetic mechanisms to prevent cancer and other age-related diseases. However, primary research publications on genetic and molecular mechanisms of aging in the bowhead whale are scarce, consisting primarily of genome and transcriptome analysis[16–18].

The multi-stage model of carcinogenesis posits that the transition from a normal cell to a cancer cell involves multiple distinct genetic "hits," or mutations[19]. Larger and longer-living species might require greater numbers of "hits" for oncogenic transformation, given their greater cell number and increased lifespan. Indeed, there is experimental evidence to support this hypothesis. Rangarajan et al. found that while mouse fibroblasts require perturbation of 2 pathways for tumorigenic transformation (p53 and

bioRxiv preprint doi: https://doi.org/10.1101/2023.05.07.539748; this version posted May 8, 2023. The copyright holder for this preprint (which was not certified by peer review) is the author/funder, who has granted bioRxiv a license to display the preprint in perpetuity. It is made available under aCC-BY-NC-ND 4.0 International license.

Ras), human fibroblasts require 5 hits (p53, pRb, PP2A, telomerase and Ras)[20]. A human should thus have a dramatically lower per-cell incidence of malignant transformation than a mouse, and can maintain a larger number of cells for a longer period of time.

Species that are larger and longer-lived than humans may be expected to have even more layers of protection against oncogenic transformation than humans and common model species. In support of this hypothesis, recent studies have identified copy number expansion and functional diversification of multiple tumor suppressor genes, such as *TP53* and *LIF*, in elephants and other taxa[3,5,21–23]. These studies identified multiple copies of *TP53* in the elephant genome, several of which were confirmed to be transcribed and translated in elephant fibroblasts and contributed to an enhanced apoptotic response to genotoxic stress.

However, additional copies of p53 genes are unlikely to slow down aging. One promising mechanism that could help explain both cancer resistance and slower aging in long-lived mammals is more accurate or efficient DNA repair. Genetic mutations have been identified as causal factors in carcinogenesis for over a century[24]. Perhaps one of the most compelling lines of evidence supporting the role of DNA repair in the pathogenesis of aging and cancer comes from studies of mutants with accelerated aging phenotypes. Remarkably, most such mutants have defects in DNA repair enzymes[25–29]. Across species, several studies have also pointed toward improved DNA repair capacity and reduced mutation accumulation as characteristics associated with species longevity[30–34]. Here, we identify specific cellular and molecular traits characterizing bowhead cancer resistance and longevity and distinguishing the

bioRxiv preprint doi: https://doi.org/10.1101/2023.05.07.539748; this version posted May 8, 2023. The copyright holder for this preprint (which was not certified by peer review) is the author/funder, who has granted bioRxiv a license to display the preprint in perpetuity. It is made available under aCC-BY-NC-ND 4.0 International license.

bowhead from shorter-lived mammals including humans. We show that bowhead whale cells are not more prone to apoptosis or require more genetic hits for malignant transformation than human cells. Instead, bowhead whale relies on more accurate and efficient DNA double strand break (DSB) repair mediated by CIRBP and RPA2. This more "conservative" strategy that does not needlessly eliminate cells but repairs them, may be critical for the long and cancer-free lifespan of the bowhead whale.

Results

Growth characteristics, cellular senescence, and cell death in bowhead whale

Most human somatic cells lack telomerase activity and as a result undergo replicative senescence with serial passaging in culture[35]. Replicative and stress-induced senescence are important mechanisms for preventing cancer. Using TRF and TRAP assays to measure telomere length and telomerase activity, we found that bowhead whale skin fibroblasts, like human fibroblasts, lack telomerase activity and experience telomere shortening followed by replicative senescence with passaging in culture (Figure 1a, b). In both species, nearly all cells stained positive for senescence-associated β-galactosidase upon terminal growth arrest (Figure 1c, d). As in human fibroblasts, stable overexpression of human telomerase reverse transcriptase (*hTERT)* to maintain telomere length prevented replicative senescence in bowhead cells (Figure 1a). Senescence can also be induced by DNA damage. Like human cells, bowhead whale skin fibroblasts efficiently entered senescence but did not significantly induce cell death in response to 10 or 20 Gy of γ-irradiation (Figure 1c-e).

bioRxiv preprint doi: https://doi.org/10.1101/2023.05.07.539748; this version posted May 8, 2023. The copyright holder for this preprint (which was not certified by peer review) is the author/funder, who has granted bioRxiv a license to display the preprint in perpetuity. It is made available under aCC-BY-NC-ND 4.0 International license.

Interestingly, transcriptome analysis of human and bowhead whale senescent fibroblasts showed reduced induction of senescence-associated secretory phenotype (SASP) factors in bowhead whale (Figure 1f) relative to human. Paracrine effects of SASP on surrounding cells are thought to contribute to age-related diseases and carcinogenesis. These transcriptomic differences may indicate that senescence is able to preserve its anti-cancer function in the bowhead with reduced harmful paracrine signaling.

To test whether increased p53 activity could contribute to cancer resistance in the bowhead whale, we transiently transfected primary mouse, cow, human and bowhead whale skin fibroblasts with a luciferase reporter vector containing a p53-response element. The bowhead whale cells had the lowest p53 activity of the species tested (Figure 1g). Additionally, we did not observe any differences in the induction of apoptosis in response to UVC between species (Figure 1h). Together, our results argue against the idea that increased clearance of damaged cells through apoptosis contributes to cancer resistance in the bowhead whale.

Requirements for oncogenic transformation of bowhead whale cells

We initially identified a minimal combination of oncogene and tumor suppressor hits required for *in vitro* malignant transformation of bowhead whale skin fibroblasts using the soft agar assay, which measures anchorage-independent growth, a hallmark of cancer. While normal cells undergo growth arrest or programmed cell death (anoikis) in soft agar, malignant cells continue to grow without substrate adhesion and form visible colonies[36]. We introduced constructs targeting oncogene and tumor suppressor pathways into primary skin fibroblasts with PiggyBac (PB) transposon vectors, which

bioRxiv preprint doi: https://doi.org/10.1101/2023.05.07.539748; this version posted May 8, 2023. The copyright holder for this preprint (which was not certified by peer review) is the author/funder, who has granted bioRxiv a license to display the preprint in perpetuity. It is made available under aCC-BY-NC-ND 4.0 International license.

integrate into the genome and drive stable expression. Since bowhead whale primary fibroblasts, like human fibroblasts, exhibit progressive telomere shortening and lack telomerase activity (Figure 1b), we used cell lines expressing (*hTERT*) to bypass replicative senescence.

In agreement with published findings, transformation of human *hTERT*+ fibroblasts required combined expression of H-Ras^{G12V}, SV40 Large T (LT) antigen (which binds and inactivates p53 and the Rb family of tumor suppressors), and SV40 Small T (ST) antigen (which binds and inactivates PP2A) (Figure 2a)[20]. Rather than requiring hits to additional pathways, however, bowhead *hTERT*+ fibroblasts were transformed by H-Ras^{G12V} and SV40 LT alone, suggesting that bowhead cells may require fewer genetic mutations to become cancerous compared to human cells (Figure 2a). These findings were supported by mouse xenograft assays, in which the number of hits needed for tumor growth matched the findings from soft agar (Figure 2b).

We next sought to confirm these findings at the genetic level, through CRISPR editing of individual tumor suppressor genes in bowhead fibroblasts. While the sequenced bowhead genome has not revealed copy number expansion of canonical tumor suppressor genes[16,17], CRISPR knockout allows for more precise quantification of the number of genetic mutations required for oncogenesis. While the most important target of SV40 LT is thought to be Rb (*RB1* gene), it is also known to inactivate p130 and p107, two additional members of the Rb-family, providing some level of functional redundancy. Using CRISPR, we were able to introduce targeted mutations into the bowhead *RB1* gene specifically, along with *TP53* (the other target of LT), and *PTEN* (an upstream inhibitor of Akt signaling commonly mutated in human cancers, and operating

bioRxiv preprint doi: https://doi.org/10.1101/2023.05.07.539748; this version posted May 8, 2023. The copyright holder for this preprint (which was not certified by peer review) is the author/funder, who has granted bioRxiv a license to display the preprint in perpetuity. It is made available under aCC-BY-NC-ND 4.0 International license.

in the same pathway as PP2A). Following transfection of *hTERT*+ bowhead fibroblasts with Cas9-guide RNA ribonucleoprotein complexes targeting each of the aforementioned genes, we screened clonally isolated colonies for loss of the targeted protein by Western blot (Figure 2c, d, Extended Data Figure 1a, b). We additionally screened the colonies with luciferase reporter assays to confirm loss of protein function and activity (Extended Data Figure 1c, d). For each selected clone, we sequenced the CRISPR-targeted genes to confirm homozygous knockout at the genetic level and determine the causal mutations (Supplementary Figure 1, 2). Through this strategy, we generated single and compound homozygous knockout bowhead whale fibroblasts for *TP53*, *RB1*, and *PTEN*. In agreement with our initial findings, genetic inactivation of *TP53* and *RB1* in bowhead whale fibroblasts expressing *hTERT* and H-Ras^{G12V} was sufficient for malignant transformation in both soft agar and mouse xenograft assays (Figure 2a, b). These findings suggest that despite its large size and long lifespan, the cells of the bowhead whale unexpectedly require fewer mutational hits for malignant transformation than human cells.

Excision repair and mutagenesis in the bowhead whale

To understand if improved DNA repair might reduce cancer risk in the bowhead whale, we first assessed the efficiency of nucleotide excision repair (NER) and base excision repair (BER) in bowhead whale cells. NER is primarily responsible for removing helix-distorting DNA lesions. To quantify NER activity, we utilized a host cell plasmid reactivation assay and quantitation of cyclobutane pyrimidine dimers by ELISA to measure repair of UVC-induced DNA damage. NER efficiency was similar between bowhead and human (Extended Data Figure 2a, b). BER is responsible for ameliorating

bioRxiv preprint doi: https://doi.org/10.1101/2023.05.07.539748; this version posted May 8, 2023. The copyright holder for this preprint (which was not certified by peer review) is the author/funder, who has granted bioRxiv a license to display the preprint in perpetuity. It is made available under aCC-BY-NC-ND 4.0 International license.

many types of spontaneous DNA base damage such as oxidation and deamination. The efficiency of BER, as measured by plasmid reactivation assay, trended toward higher BER activity in bowhead whale compared to human cells, but this difference was not statistically significant (Extended Data Figure 2c). Additionally, bowhead fibroblasts displayed dramatically higher PARP activity in response to H_2O_2 treatment (Extended Data Figure 2d, e). PARP proteins play important roles in the DNA damage response and are recruited to sites of DNA damage where they participate in the DNA damage response and in repair.

We next compared the point mutation frequency in the bowhead whale and human using the HPRT mutagenesis assay, which relies on loss of HPRT activity after mutagen treatment[37]. The *HPRT* gene exists as a single copy on the X chromosome in male mammalian cells, a feature we found to be true for the bowhead as well (see Methods). We treated primary fibroblast lines from male bowhead whale and human with the potent mutagen and alkylating agent N-ethyl-N-nitrosourea (ENU), and then plated cells in selective media containing 6-thioguanine, which kills cells with functional HPRT. Despite a slightly higher sensitivity to ENU in bowhead whale as indicated by colony-forming efficiency in non-selective media, the rate of HPRT mutant colony formation was markedly lower in bowhead whale than human fibroblasts, an effect which remained significant after adjusting for plating efficiency (Extended Data Figure 2f, g). This result suggests that bowhead whale has more accurate DNA repair.

High efficiency and fidelity of bowhead whale double-strand break repair

DNA DSBs are toxic if not repaired and may lead to mutations through inaccurate repair. DSBs are repaired by two major pathways: non-homologous end joining (NHEJ)

bioRxiv preprint doi: https://doi.org/10.1101/2023.05.07.539748; this version posted May 8, 2023. The copyright holder for this preprint (which was not certified by peer review) is the author/funder, who has granted bioRxiv a license to display the preprint in perpetuity. It is made available under aCC-BY-NC-ND 4.0 International license.

and homologous recombination (HR). To assess relative NHEJ efficiency, we integrated fluorescent GFP-based reporter cassettes[38] into fibroblasts from mouse, cow, human and bowhead whale. Following DSB induction with I-SceI, we observed markedly elevated NHEJ efficiency in bowhead whale relative to other species (Figure 3a, Extended Data Figure 3a-c). Additionally, bowhead whale fibroblasts accumulated fewer micronuclei, a marker of chromosomal instability, after 2Gy γ-irradiation (Figure 3b, Extended Data Figure 3d). The kinetics of radiation-induced DSB rejoining as measured by pulsed-field gel electrophoresis were similar between bowhead and human cells, with almost all breaks repaired within 48h in both species (Extended Data Figure 3e, f).

As mutations resulting from inaccurate DSB repair promote cancer development, we next sought to assess the fidelity of DSB repair in the bowhead whale. Sequencing and analysis of repair junctions from integrated NHEJ reporter (Figure 3) and extra-chromosomal NHEJ reporter (Extended Data Figure 3a, c) assays showed higher fidelity of NHEJ in bowhead whale cells: compared to human, the bowhead whale is less prone to producing deletions during the repair of incompatible DNA termini and far more frequently joins ends without deleting any bases beyond the small overhang region.

We also measured the fidelity of repair at an endogenous genomic locus. Initial sequencing results from CRISPR tumor suppressor knockout experiments suggested a strong bias in bowhead whale cells toward DSB repair products with single-base insertion mutations, in contrast to the greater diversity and size of repair outcomes commonly observed in human and mouse cells. To systematically compare mutational outcomes of CRISPR break repair in the bowhead whale to those of humans and

bioRxiv preprint doi: https://doi.org/10.1101/2023.05.07.539748; this version posted May 8, 2023. The copyright holder for this preprint (which was not certified by peer review) is the author/funder, who has granted bioRxiv a license to display the preprint in perpetuity. It is made available under aCC-BY-NC-ND 4.0 International license.

shorter-living mammals, we performed CRISPR transfections in multiple primary fibroblast lines from bowhead whale, human, cow, and mouse, and used deep amplicon sequencing of the targeted locus to generate detailed profiles of repair outcomes. We took advantage of the fact that exon 1 of the *PTEN* tumor suppressor gene is highly conserved across mammals, with 100% sequence identity across included species (Extended Data Figure 4a). We were therefore able to examine species-specific DSB repair outcomes at an endogenous genomic locus while minimizing intra-species variation in the break-proximal sequence context.

Analysis of sequencing data revealed species-specific repair outcomes, which were consistent across cell lines derived from multiple animals of each species (Figure 3d-f). In human, cow, and mouse, the most common mutational outcomes were deletions. In contrast, the bowhead was the only species that preferentially repaired breaks with a single-base insertion. The frequency of unmodified alleles, which are known to occur after error-free repair of CRISPR DSBs[39,40], was the highest in bowhead whale (Figure 3e). No insertions or deletions were detected in untreated control samples (Extended Data Figure 4b). As analysis of CRISPR RNP transfection efficiency by flow cytometry and cleavage efficiency by digital droplet PCR showed similar CRISPR efficiencies across species (Extended Data Figure 5a, Supplementary Figure 3a, b), differences in the unmodified allele fraction most likely result from differences in repair fidelity. While small indels predominated in all species, we observed a marked inverse correlation between the frequency of large deletions and species lifespan, with the bowhead producing fewer large deletions than human, cow, and mouse (Figure 3d-f). When we assigned frequency-based percentile ranks from most negative to most positive indel

bioRxiv preprint doi: https://doi.org/10.1101/2023.05.07.539748; this version posted May 8, 2023. The copyright holder for this preprint (which was not certified by peer review) is the author/funder, who has granted bioRxiv a license to display the preprint in perpetuity. It is made available under aCC-BY-NC-ND 4.0 International license.

size (largest deletions to largest insertions), we observed a strong correlation between species lifespan and 5th percentile indel size, corresponding to large deletions (Pearson's *r*=0.85, p=0.0009) (Extended Data Figure 6). The results from these experiments suggest a greater efficiency and accuracy of DSB repair in the bowhead whale relative to humans and other mammals.

CIRBP contributes to high DSB repair efficiency in the bowhead whale

To identify mechanisms contributing to the efficiency and accuracy of DSB repair in the bowhead whale, we measured and compared expression of DNA repair proteins in the bowhead to other mammalian species by Western blot, quantitative MS proteomics, and RNA seq (Figure 4a, Extended Data Figure 7a-d). Bowhead cells showed strikingly higher abundance of cold-inducible RNA-binding protein (CIRBP) than other mammalian species. (Figure 4a, Extended Data Figure 7a, d). Levels of PARP1, a functional partner of CIRBP during DNA repair[41], were also increased relative to human. Unexpectedly, we found that levels of several important canonical NHEJ proteins (e.g. Ku70, Ku80, DNA-PKcs) are substantially higher in human cells than any other species tested (Figure 4a, Extended Data Figure 7a).

CIRBP is an RNA- and PAR-binding protein whose expression is induced by a variety of cellular stressors including cold shock, hypoxia, and UV irradiation[41–44]. It binds the 3' UTR of mRNAs that encode proteins involved in cellular stress and DNA damage responses and promotes their stability and translation: known targets include ATR, RPA2, thioredoxin, and p27[45–48]. There is also evidence for a more direct role of CIRBP in DNA repair: PARP-1-dependent localization of CIRBP to sites of DNA damage promotes DSB repair and antagonizes micronucleus formation[41].

bioRxiv preprint doi: https://doi.org/10.1101/2023.05.07.539748; this version posted May 8, 2023. The copyright holder for this preprint (which was not certified by peer review) is the author/funder, who has granted bioRxiv a license to display the preprint in perpetuity. It is made available under aCC-BY-NC-ND 4.0 International license.

To test whether CIRBP contributes to efficient NHEJ in bowhead whale cells, we overexpressed human (hCIRBP) and bowhead whale (bwCIRBP) in human NHEJ reporter cells. Overexpression of bwCIRBP, but not hCIRBP, enhanced NHEJ efficiency in human cells ~1.6-fold (p=0.002) and in mouse embryonic fibroblasts ~3-fold (Figure 4b, Extended Data Figure 8a). Overexpression of bwCIRBP, but not hCIRBP, also increased HR efficiency in human cells ~2-fold (Figure 4c, e). Conversely, CIRBP depletion in bowhead whale cells by siRNA significantly reduced NHEJ efficiency (p=0.032) (Figure 4d, e). Consistent with published observations, overexpression of bwCIRBP with nine arginines in the repeated RGG motif mutated to alanine (9R/A), which impairs CIRBP's ability to bind to PAR-polymers[41], failed to stimulate HR and reduced stimulation of NHEJ (Figure 4b, c, e). To test the effects of bwCIRBP overexpression on chromosomal stability, we quantified formation of micronuclei in human cells after γ-irradiation. We found that overexpression of bwCIRBP significantly decreased the percentage of cells with micronuclei, reflecting an improvement in genomic stability (Figure 4f).

Surprisingly, we observed during our experiments that CIRBP protein abundance in the bowhead remained high regardless of whether cells were cultured at 37°C, 33°C, or lower temperatures (the core body temperature of the bowhead has been measured at 33.8°C)[49,50], suggesting constitutive expression in contrast to its strong temperature dependence in other mammals (Extended Data Figure 8b)[42]. At no temperature did human cells produce similarly high CIRBP levels. In contrast, RNA-seq analysis (verified by qPCR) showed nearly identical CIRBP transcript levels between human and bowhead whale fibroblasts (Extended Data Figure 7b, 8c). The discrepancy between

bioRxiv preprint doi: https://doi.org/10.1101/2023.05.07.539748; this version posted May 8, 2023. The copyright holder for this preprint (which was not certified by peer review) is the author/funder, who has granted bioRxiv a license to display the preprint in perpetuity. It is made available under aCC-BY-NC-ND 4.0 International license.

mRNA and protein levels in tested species agrees with previous findings of CIRBP regulation at the post-transcriptional level[51,52] .

The human and bowhead CIRBP proteins differ by only 5 C-terminal amino acids (Extended Data Figure 9a, b). Substitution of these 5 codons in hCIRBP with bowhead codons increased protein expression, while mutation of bwCIRBP with the 5 hCIRBP codons decreased it (Extended Data Figure 9c). This was not accompanied by changes in mRNA transcript levels, consistent with post-transcriptional regulation (Extended Data Figure 9d). Interestingly, although CIRBP abundance increased following introduction of the 5 bowhead substitutions to hCIRBP, it did not achieve the expression of bowhead CIRBP, suggesting that synonymous changes to the mRNA coding sequence contribute to higher translation efficiency of bowhead whale CIRBP. Consistent with this notion, bwCIRBP has a higher codon adaptation index (CAI)[53] than hCIRBP; this difference remains after introduction of the five reciprocal mutations (Extended Data Figure 9e).

To test whether a hypothermia-mediated increase in human CIRBP can also affect DSB repair efficiency, we kept human cells for two days at 33°C before transfection with NHEJ reporter plasmid pre-digested with I-Sce-1. Indeed, cells exposed to hypothermia showed a ~2-fold ($p=0.0017$) increase in NHEJ efficiency (Figure 4g).

Mechanisms of bowhead whale DNA repair fidelity

LC-MS proteomics data and Western blots with multiple antibodies suggested increased abundance of the single-stranded DNA binding protein RPA2 in the bowhead whale (Figure 4a, Extended Data Figure 7a, c). This was paralleled by elevated RPA2 transcript abundance (Extended Data Figure 7b). RPA is a conserved heterotrimeric

bioRxiv preprint doi: https://doi.org/10.1101/2023.05.07.539748; this version posted May 8, 2023. The copyright holder for this preprint (which was not certified by peer review) is the author/funder, who has granted bioRxiv a license to display the preprint in perpetuity. It is made available under aCC-BY-NC-ND 4.0 International license.

ssDNA-binding protein complex required for eukaryotic DNA replication, which plays a critical role in DNA repair and DNA damage signaling[54,55]. RPA deficiency increases the frequency of DSBs under both basal[56] and stressed[57] conditions. Conversely, RPA overexpression increases resistance to genotoxic insults[57–60]. RPA promotes NHEJ *in vitro*[61], can protect ssDNA overhangs at Ku-bound DSBs[62,63], and antagonizes microhomology-mediated end joining[6448,49].

It has previously been shown that RPA2 is an unstable protein highly prone to oxidative damage, and that the abundance of this subunit affects the abundance of RPA1 and RPA3[65,66]. We therefore sought to determine whether the high abundance of RPA2 in bowhead whale cells may contribute to DNA repair fidelity. Because RPA is required for cell viability, and can cause toxicity when not expressed with appropriate subunit stoichiometry[67], we selected methods aimed at transiently increasing or decreasing RPA activity in the period surrounding break induction to specifically isolate effects on DSB repair fidelity. Treatment of cells transfected with CRISPR to induce DSBs with the small-molecule RPA DNA-binding inhibitor TDRL-505[68] significantly increased indel rates in both bowhead and human fibroblasts (Figure 5a, b). In bowhead, RPA inhibition also increased the frequency of larger deletions, although this difference did not reach significance (Figure 5b). Conversely, co-transfection of trimeric recombinant human RPA protein during CRISPR significantly decreased the frequency of mutated alleles in human cells without affecting CRISPR RNP transfection efficiency (Figure 5a, Supplementary Figure 3c). We additionally tested the effect of bwCIRBP overexpression on repair fidelity in human cells and observed a modest but significant reduction in indel rates (Figure 5c). These results support the notion that variations in

bioRxiv preprint doi: https://doi.org/10.1101/2023.05.07.539748; this version posted May 8, 2023. The copyright holder for this preprint (which was not certified by peer review) is the author/funder, who has granted bioRxiv a license to display the preprint in perpetuity. It is made available under aCC-BY-NC-ND 4.0 International license.

CIRBP and RPA2 abundance, affect the fidelity of DSB repair and promote genomic stability in the bowhead whale.

Discussion

By studying a mammal capable of maintaining its health and avoiding death from cancer for over 2 centuries, we are offered a unique glimpse behind the curtain of a global evolutionary experiment that tested more mechanisms affecting cancer and aging than humans could ever hope to approach. Through experiments using primary fibroblasts from the bowhead whale, we experimentally determined genetic requirements for oncogenic transformation in the world's longest living mammal, and provide evidence that additional tumor suppressors are not the only solution to Peto's Paradox. Instead, we find that the bowhead whale solution lies upstream of tumor suppressor loss, and is defined by a capacity for highly accurate DNA DSB repair. We also present evidence that two proteins, RPA2 and CIRBP, are highly expressed in the bowhead relative to other mammals and contribute to more efficient and accurate DSB repair.

When cells experience DNA breaks, they are faced with a choice between several different fates, which cooperate to balance short-term risks to organismal viability with the long-term risks of genome instability. One option is resolution of the DNA damage response and resumption of cell function. While an unrepaired DSB is sufficient to kill a cell, an inaccurately repaired DSB can give rise to a cancer that kills the entire organism. The magnitude of this threat is reflected in the diversity of checkpoint mechanisms mammals have evolved to arrest or eliminate cells with DNA damage.

bioRxiv preprint doi: https://doi.org/10.1101/2023.05.07.539748; this version posted May 8, 2023. The copyright holder for this preprint (which was not certified by peer review) is the author/funder, who has granted bioRxiv a license to display the preprint in perpetuity. It is made available under aCC-BY-NC-ND 4.0 International license.

Thus, persistent or excessive damage signaling can trigger a second category of DNA damage outcomes: apoptosis or senescence.

Prompt and efficient DSB repair promotes the survival and continued function of somatic cells. Ideally, this results in faithful restoration of the original genomic sequence. However, aberrant outcomes such as loss of chromosome fragments (e.g. micronuclei), chromosomal rearrangements, or large deletions cause massive changes to the original DNA sequence[69]. These forms of genome instability are hallmarks of cancer and core drivers of malignant transformation. In quiescent cell populations, there is increased potential for accumulation of persistent unrepaired DSBs. Efficient repair of DSBs is particularly important for permanently post-mitotic cells like neurons and cardiomyocytes, which often are not replaced after cell death. Ultimately, the value of DSB repair to an organism's survival is a function of both accuracy and efficiency. Upon excessive damage, it is often better for organismal survival and longevity to eliminate cells at risk of genomic instability through apoptosis or senescence.

Senescence is an important mechanism to control cells with potential genome instability through permanent growth arrest. Telomere shortening functions to induce senescence by limiting the number of times a cell can replicate. This mechanism appears to be functional in bowhead whale fibroblasts, in line with the theory that telomere shortening is prevalent as a cancer-prevention mechanism in large-bodied mammals[70]. An additional such mechanism was recently reported for the bowhead whale in the form of a *CDKN2C* checkpoint gene duplication[71]. Senescence in general appears to represent a tradeoff between cancer and other forms of age-related dysfunction. There is substantial evidence for harmful paracrine effects of senescence through the pro-

bioRxiv preprint doi: https://doi.org/10.1101/2023.05.07.539748; this version posted May 8, 2023. The copyright holder for this preprint (which was not certified by peer review) is the author/funder, who has granted bioRxiv a license to display the preprint in perpetuity. It is made available under aCC-BY-NC-ND 4.0 International license.

inflammatory SASP[72]. Here we demonstrate that bowhead whale has reduced inflammatory components of the SASP, which could reduce the negative impact of senescence.

Like senescence, apoptosis is an efficient and critical mechanism to reduce the number of cells with dangerous levels of genome instability. Its importance as a cancer prevention mechanism is evident from the prevalence of p53 mutations in cancer[73] and supported by findings of enhanced p53 function in the elephant[3–5]. However, high rates of apoptosis are likely to accelerate age-related decline through permanent cell loss[74], especially in post-mitotic and irreplaceable cell populations in tissues such as brain and heart. Because excessive cell death or arrest is incompatible with organismal survival, baseline levels of DNA damage must be repaired. Given that most cells in mammalian bodies experience multiple endogenous DSBs per day[75], faithful repair of these breaks is critical.

Why might the bowhead whale have evolved improved DNA repair, as opposed to the increased tumor suppressor copy number and elevated apoptotic response found in the elephant and often proposed as a solution to Peto's Paradox? One possible explanation is that tumor suppressors, apoptosis, and senescence all appear to pose costs to the organism and represent tradeoffs between cancer and stem cell depletion leading to age-related degeneration. Simply shifting the balance from apoptosis/senescence to survival and repair could be detrimental if not also coupled with increased fidelity, as evidenced by the frequent upregulation of DNA repair pathways in cancer cells[76]. However, evolutionary improvements that couple high efficiency with high fidelity, as found in the bowhead whale, would promote long-term tissue function and maintenance

bioRxiv preprint doi: https://doi.org/10.1101/2023.05.07.539748; this version posted May 8, 2023. The copyright holder for this preprint (which was not certified by peer review) is the author/funder, who has granted bioRxiv a license to display the preprint in perpetuity. It is made available under aCC-BY-NC-ND 4.0 International license.

427 at both the cellular and genomic levels. Efficient repair could reduce loss of valuable
428 post-mitotic cells with age and reduce mutations in dividing cells. Maintenance of
429 genome stability would reduce cancer risk and - as suggested by a rapidly growing body
430 of evidence implicating age-related somatic mosaicism as a ubiquitous feature and
431 functional driver of aging[77–81]- likely also protect against numerous other aspects of age-
432 related decline. Thus, the lower accuracy and efficiency of DSB repair observed in
433 mammals with shorter lifespans may simply reflect an absence of sufficient selective
434 pressure. One potential drawback of a very accurate DNA repair system is a reduction
435 in diversity and slower rate of evolution of new traits. However, species living in safe
436 and stable environments have no evolutionary pressure to rapidly evolve new
437 adaptations. Interestingly, genome analysis of long-lived rockfishes living in deep ocean
438 revealed positive selection in DNA repair pathways[82].

439 The evolution of constitutively high CIRBP expression in the bowhead whale is likely to
440 have been driven, at least in part, by the unique physiological stresses this Arctic
441 cetacean must endure. This naturally includes the extremely cold water in which it is
442 constantly immersed, but also the ischemia/reperfusion-like fluctuations in tissue
443 oxygen concentrations experienced by diving mammals[83].

444 Interestingly, beneficial effects of cold as a therapeutic agent have been known for a
445 long time with brief cold-water immersion believed to promote health and hardening in
446 Nordic cultures. Currently, whole body cryotherapy is widely used in sports medicine to
447 reduce inflammation and facilitate recovery after exercise or injury[84]. While molecular
448 mechanisms responsible for the beneficial effects of cryotherapy are largely unknown,

bioRxiv preprint doi: https://doi.org/10.1101/2023.05.07.539748; this version posted May 8, 2023. The copyright holder for this preprint (which was not certified by peer review) is the author/funder, who has granted bioRxiv a license to display the preprint in perpetuity. It is made available under aCC-BY-NC-ND 4.0 International license.

we speculate that increased CIRBP expression may contribute to health benefits by facilitating DNA repair.

Cold showers provide a mild and transient reduction in body temperature, whereas artificial reduction of body temperature, or therapeutic hypothermia, is used clinically during surgery[85]. Interestingly, recovery from therapeutic hypothermia is compromised in CIRBP-KO rats and improved in rats with transgenic CIRBP overexpression[86]. Similar protective effects of CIRBP during hypothermia have been reported in brain[87], kidney[88] intestine[89], and cold-preserved hearts[90]. Given the dramatically enhanced protein production driven by bwCIRBP and hCIRBP mutants, local delivery of such CIRBP variants (e. g. through mRNA/DNA vector injection) could hold promise as strategies to improve tissue recovery from surgery or organ transplant.

There are currently no approved therapeutics which aim to bolster DNA repair for the prevention of cancer or age-related decline, and it has been suggested that DNA repair would be difficult or impossible to improve[91]. However, the bowhead whale provides evidence that this notion is incorrect. Therapeutics based on increasing the activity or abundance of proteins like CIRBP or RPA2 could one day enable the treatment of genome instability as a modifiable disease risk factor.

Acknowledgements

We would like to thank the researchers at the North Slope Borough Department of Wildlife Management, the Alaska Eskimo Whaling Commission, and the Iñupiaq community of Barrow for generously sharing bowhead whale samples, time, resources,

bioRxiv preprint doi: https://doi.org/10.1101/2023.05.07.539748; this version posted May 8, 2023. The copyright holder for this preprint (which was not certified by peer review) is the author/funder, who has granted bioRxiv a license to display the preprint in perpetuity. It is made available under aCC-BY-NC-ND 4.0 International license.

skill, and knowledge, and without whom the above work would not have been possible.

This work was supported by grants from US National Institutes on Aging to VNG, ZZ, JV, AS and VG, and by an award from the Milky Way Research Foundation to VG.

Author contributions

VG, AS, DF, MZ designed research; DF analyzed senescence, DNA repair, CIRBP with help from SAB, AP, EH, AW, NM; MZ conducted tumor suppressor CRISPR experiments, RPA experiments, HPRT assays, and assessed DNA repair fidelity using CRISPR with help from SB, MS, NH; XT analyzed tumorigenicity; YZ and AG assisted with mouse tumor studies; JCG, TLS, MZ, DF collected bowhead specimens; MZ, GT performed proteomics; ML analyzed micronuclei; JYL analyzed SASP; VG, ZZ, JV contributed data analysis and conceptualization; VG and AS obtained funding and supervised the study; MZ, DF, AS and VG wrote the manuscript with input from all authors.

Competing interests

The authors declare no competing interests.

bioRxiv preprint doi: https://doi.org/10.1101/2023.05.07.539748; this version posted May 8, 2023. The copyright holder for this preprint (which was not certified by peer review) is the author/funder, who has granted bioRxiv a license to display the preprint in perpetuity. It is made available under aCC-BY-NC-ND 4.0 International license.

Methods

Reagents

Detailed information on reagents, such as antibodies and sequences of primers, probes, CRISPR guides, and siRNAs, is provided in Supplementary Methods.

Animal experiments

All animal experiments were approved and performed under pre-approved protocols and in accordance with guidelines set by the University of Rochester Committee on Animal Resources (UCAR).

Whale sample collection

Bowhead whale tissues were obtained from adult bowhead whales (*Balaena mysticetus*) captured during 2014 and 2018 Iñupiaq subsistence harvests in Barrow (Utqiaġvik), AK, in collaboration with the North Slope Borough Department of Wildlife Management (NSB DWM) and Alaska Eskimo Whaling Commission after signing a Memorandum of Understanding (September 2014 and March 2021). Tissues were sampled immediately after bowhead whales were brought ashore, after permission to sample was given by the whaling captain, and explants kept in culture medium on ice or at 4°C through initial processing and shipping until arrival at the University of Rochester (UR) for primary fibroblast isolation from skin and lung. Transfer of bowhead whale samples from NSB DWM to UR was under NOAA/NMFS permit 21386.

Primary cell cultures

bioRxiv preprint doi: https://doi.org/10.1101/2023.05.07.539748; this version posted May 8, 2023. The copyright holder for this preprint (which was not certified by peer review) is the author/funder, who has granted bioRxiv a license to display the preprint in perpetuity. It is made available under aCC-BY-NC-ND 4.0 International license.

Primary skin fibroblasts were isolated from skin (dermal) tissues as previously described.[92] Briefly, skin tissues were shaved and cleaned with 70% ethanol. Tissues were minced with a scalpel and incubated in DMEM/F-12 medium (ThermoFisher) with Liberase™ (Sigma) at 37ºC on a stirrer for 15-90 min. Tissues were then washed and plated in DMEM/F-12 medium containing 12% fetal bovine serum (GIBCO) and Antibiotic-Antimycotic (GIBCO). All subsequent maintenance culture for fibroblasts from bowhead and other species was in EMEM (ATCC) supplemented with 12% fetal bovine serum (GIBCO), 100 units/mL penicillin, and 100 mg/mL streptomycin (GIBCO). All primary cells were cultured at 37ºC with 5% CO_2 and 3% O_2 except bowhead whale cells, which were cultured at 33ºC with 5% CO_2 and 3% O_2 based on published field measurements of bowhead body temperature, which measured a core temperature of 33.8 ºC and a range of lower temperatures in muscle and peripheral tissue.[49,50] Prior to beginning experiments with bowhead whale fibroblasts, optimal growth and viability conditions were empirically determined through testing of alternative temperatures, serum concentrations, and cell culture additives, with optimal culture medium found to be the same for bowhead and other species. Following isolation, low population-doubling (PD) primary cultures were preserved in liquid nitrogen, and PD was continually tracked and recorded during subsequent use for experiments.

Soft agar assay

Fibroblast culture medium as described above was prepared at 2X concentration using 2X EMEM (Lonza). To prepare the bottom layer of agar plates, 2X medium was mixed with a sterile autoclaved solution of 1.2% Noble Agar (Difco) at a 1:1 volumetric ratio, and 3 mL of 1X medium/0.6% agar was pipetted into each 6-cm cell culture dish and

bioRxiv preprint doi: https://doi.org/10.1101/2023.05.07.539748; this version posted May 8, 2023. The copyright holder for this preprint (which was not certified by peer review) is the author/funder, who has granted bioRxiv a license to display the preprint in perpetuity. It is made available under aCC-BY-NC-ND 4.0 International license.

allowed to solidify at room temperature in a tissue culture hood. To plate cells into the upper layer of soft agar, cells were harvested and washed, and immediately prior to plating were resuspended in 2X medium at 20,000 cells/1.5 mL and diluted twofold in 0.8% Noble Agar pre-equilibrated to 37°C. The cells in 0.4% agar/1X medium were pipetted gently to ensure a homogeneous single cell suspension, and 3 mL (20,000 cells) per 6 cm dish were layered on top of the solidified lower layer. After solidifying in tissue culture hoods for 20-30 min, additional medium was added to ensure the agar layers were submerged, and dishes were moved into cell culture incubators. Fresh medium was added onto the agar every 3 days. 4 weeks after plating, viable colonies were stained overnight with nitro blue tetrazolium chloride (Thermo Fisher) as previously described.[36] All cell lines were plated in triplicate.

Mouse xenograft assay

NIH-III nude mice (Crl:NIH-Lystbg-J Foxn1nuBtkxid) were purchased from Charles River Laboratories Inc. (Wilmington, MA, USA). Seven-week-old female mice were used to establish xenografts. For each injection, 2×10^6 cells were harvested and resuspended in 100 µl of ice-cold 20% matrigel (BD Bioscience, Franklin Lakes, NJ) in PBS (Gibco). Mice were anesthetized with isoflurane gas, and 100 µl solution per injection was injected subcutaneously into the right and left flanks of each mouse with a 22 gauge needle. 3 mice were injected bilaterally, for a total of 6 injections, per cell line tested. Tumor length and width were measured and recorded every 3-4 days. Mice were euthanized after reaching a predetermined humane tumor burden endpoint of a maximum tumor dimension of 20mm in diameter, determined by the longest dimension of the mouse's largest tumor. For mice that did not reach tumor burden endpoints,

bioRxiv preprint doi: https://doi.org/10.1101/2023.05.07.539748; this version posted May 8, 2023. The copyright holder for this preprint (which was not certified by peer review) is the author/funder, who has granted bioRxiv a license to display the preprint in perpetuity. It is made available under aCC-BY-NC-ND 4.0 International license.

experiments were terminated and mice euthanized after a maximum of 60 days. Euthanized mice were photographed and tumors were excised, photographed, and weighed to determine the mass of each tumor. Sections of each tumor were frozen at -80°C and preserved in formalin.

Telomere lengths

Telomere length was analyzed by Southern blot using the TRF method. Genomic DNA was extracted from cultured fibroblasts at different population doublings, digested with a mixture of AluI, HaeIII, RsaI, and HinfI restriction enzymes that do not cut within telomeric repeat sequences, separated using pulsed-field gel electrophoresis, and hybridized with a radiolabeled oligonucleotide containing telomeric sequence $(TTAGGG)_4$. Pulsed field gels were run using a CHEF-DR II apparatus (Bio-Rad) for 22h at a constant 45 V, using ramped pulse times from 1 to 10 s.

Telomeric repeat amplification protocol

Telomeric repeat amplification protocol assay was performed using the TRAPeze kit (Chemicon, Temecula, CA, USA) according to manufacturer instructions. Briefly, in the first step of the TRAP assay, radiolabeled substrate oligonucleotide is added to 0.5 µg of protein extract. If telomerase is present and active, telomeric repeats (GGTTAG) are added to the 3′ end of the oligonucleotide. In the second step, extended products are amplified by PCR. Telomerase extends the oligonucleotide by multiples of 6 bp, generating a ladder of products of increasing length. A human cancer cell line overexpressing telomerase as well as rodent cells were used as a positive control.

CRISPR ribonucleoprotein transfection

bioRxiv preprint doi: https://doi.org/10.1101/2023.05.07.539748; this version posted May 8, 2023. The copyright holder for this preprint (which was not certified by peer review) is the author/funder, who has granted bioRxiv a license to display the preprint in perpetuity. It is made available under aCC-BY-NC-ND 4.0 International license.

CRISPR RNP complexes were formed in vitro by incubating Alt-R™ S.p.Cas9 Nuclease V3 (Integrated DNA technologies) with tracRNA annealed to target-specific crRNA (Integrated DNA Technologies) according to manufacturer instructions. For generation of tumor suppressor knockouts, 3 RNP complexes with crRNAs targeting different sites in a single target gene were combined and Alt-R Cas9 Electroporation Enhancer (Integrated DNA Technologies) was added to transfection mixes prior to electroporation. For comparative analysis of repair fidelity, 3 µg of pmaxGFP plasmid (Lonza) was added to transfection mixes to monitor transfection efficiency. Cells were trypsinized and washed with PBS, and 1 x 10^6 cells were resuspended in 100 µL of NHDF Nucleofector Solution (Lonza). The cell suspension was then combined with the CRISPR transfection solution and gently mixed prior to electroporation on an Amaxa Nucleofector 2b (Lonza) using program U-23. For RPA inhibition, human and bowhead fibroblasts were treated with 50 uM TDRL-505 (Sigma) (diluted 1000x into culture medium from 50mM stock solution in DMSO) for 3 hours prior to CRISPR transfection and kept in medium with 50 uM TDRL-505 for 18 hours after transfection. For RPA co-transfection, 1 µg of recombinant human RPA heterotrimer (Enzymax) was added to CRISPR transfection solution immediately prior to electroporation.

Isolation of clonal cell colonies and screening for tumor suppressor knockout

Following CRISPR transfection, cells were plated at low density in 15-cm dishes to allow for the formation of isolated colonies. Once clonal colonies of sufficient size had formed, positions of well-isolated colonies were visually marked on the bottom of the cell culture dish while under a microscope using a marker. Dishes were aspirated and washed with PBS. Forceps were used to dip PYREX® 8x8 mm glass cloning cylinders

bioRxiv preprint doi: https://doi.org/10.1101/2023.05.07.539748; this version posted May 8, 2023. The copyright holder for this preprint (which was not certified by peer review) is the author/funder, who has granted bioRxiv a license to display the preprint in perpetuity. It is made available under aCC-BY-NC-ND 4.0 International license.

in adhesive Dow Corning® high-vacuum silicone grease (Millipore Sigma) and one glass cylinder was secured to the dish over each marked colony. 150 µL of trypsin was added to each cylinder and returned to the incubator. When cells had rounded up from the plate, the trypsin in each cylinder was pipetted to detach cells and each colony was added to a separate well in a 6-cm culture dish containing culture medium. After colonies were expanded and split into 2 wells per colony, one well was harvested for Western blot screening for absence of target proteins, while the remaining well was kept for further experiments.

Luciferase reporter assays for knockout verification

For p53 activity measurement, 1 x 10^6 cells of control (WT) and clonally isolated p53 KO cell lines were electroporated with 3 µg p53 firefly luciferase reporter plasmid pp53-TA-Luc (Clontech/Takara) and 0.3 ug renilla luciferase control plasmid pRL-CMV (Promega) on an Amaxa Nucleofector 2b (Lonza). 24h later, cells were treated with 200 uM etoposide (Sigma) to induce p53 activity. 24h following etoposide treatment, cells were harvested and luciferase activity of cell lysates was measured using the Dual-Luciferase Reporter Assay System (Promega) in a GloMax 20/20 Luminometer (Promega) according to manufacturer instructions.

For Rb activity measurement, 2 different reporters were tested in parallel: pE2F-TA-Luc (Clontech/Takara) to measure E2F transcriptional activity (repressed by Rb), and pRb-TA-Luc (Clontech/Takara) (promoter element directly suppressed by Rb). 1 x 10^6 cells of control (WT) and clonally isolated Rb KO cell lines were electroporated with 3 µg of either pE2F-TA-luc or pRb-TA-luc and 0.3 ug renilla luciferase plasmid on an Amaxa Nucleofector 2b (Lonza). Following transfection, cells were grown in complete medium

bioRxiv preprint doi: https://doi.org/10.1101/2023.05.07.539748; this version posted May 8, 2023. The copyright holder for this preprint (which was not certified by peer review) is the author/funder, who has granted bioRxiv a license to display the preprint in perpetuity. It is made available under aCC-BY-NC-ND 4.0 International license.

for 24h followed by serum-free medium for 24h. Cells were then harvested and luciferase activity measured as described above.

Next-generation sequencing of CRISPR repair products

72h after transfection, cells were harvested and genomic DNA was isolated with the Wizard Genomic DNA Purification Kit (Promega). DNA concentration was measured on a Nanodrop spectrophotometer and 100 ng of DNA per sample was PCR-amplified with KAPA2G Robust HotStart ReadyMix (Roche) based on findings of low PCR bias for KAPA polymerase[9394]. Primers targeted a conserved region surrounding *PTEN* exon 1 (Extended Data Figure 4a). PCR was performed according to manufacturer instructions, with an annealing temperature of 66°C for 30 cycles. To purify samples for next-generation sequencing, PCR products were electrophoresed on a 0.8% agarose gel and post-stained with SYBR Gold Nucleic Acid Gel Stain (Thermo Fisher). Gels were visualized on a blue light tray (BioRad) to minimize damage to DNA. A gel slice for each lane was excised using a scalpel, and each slice was cut to include the region ranging from just above the prominent *PTEN* PCR band down to and including the “primer dimer” region to ensure inclusion of any deletion alleles. DNA was extracted from gel slices using the QiaQuick Gel Extraction Kit (Qiagen), and triplicate PCR reaction eluates per sample were pooled for sequencing. Sample concentrations were measured by Nanodrop and adjusted as necessary prior to submission for 2x250 bp paired-end Illumina MiSeq sequencing with target depth of >40,000 reads/sample (Genewiz).

Analysis of CRISPR NGS data

bioRxiv preprint doi: https://doi.org/10.1101/2023.05.07.539748; this version posted May 8, 2023. The copyright holder for this preprint (which was not certified by peer review) is the author/funder, who has granted bioRxiv a license to display the preprint in perpetuity. It is made available under aCC-BY-NC-ND 4.0 International license.

644 FASTQ files from each sequenced sample were analyzed with both CRISPResso2,[95]
645 which uses an alignment-based algorithm, and CRISPRPic,[96] which uses a kmer-based
646 algorithm. CRISPResso2 was run using the following parameters: window size = 30,
647 maximum paired-end overlap = 500, bp excluded from left and right ends = 15,
648 minimum alignment score = 50, minimum identity score = 50, plot window size = 20. For
649 CRISPRPic analysis, SeqPrep[97] was used to merge overlapping read pairs and trim
650 adapter sequences. CRISPRPic was run on merged FASTQ sequences for each
651 sample with the following parameters: index size = 8, window size = 30.

652 **HPRT mutation assay**

653 For the HPRT mutation assay, cells used were low-passage primary dermal fibroblasts
654 from multiple species that were known to originate from male animals, to ensure single
655 copy-number of the X-linked *HPRT* gene. Each species was tested with 3 different cell
656 lines from 3 individual animals. The bowhead *HPRT* coding sequence was BLASTed
657 against bowhead genome scaffolds[16] and neighboring gene sequences were analyzed
658 to confirm mammal-typical localization of *HPRT* on the bowhead X-chromosome. Cells
659 were cultured in standard fibroblast growth medium, but with FBS being replaced with
660 dialyzed FBS (Omega Scientific, Inc.) and supplemented with Fibroblast Growth Kit
661 Serum-Free (Lonza) to improve growth and viability in dialyzed FBS. Dialyzed FBS was
662 found in optimization experiments to be necessary for efficient 6-thioguanine selection.
663 Prior to mutagenesis, cells were cultured for 7 days in medium containing HAT
664 Supplement (Gibco) followed by 4 days in HT Supplement (Gibco) to eliminate any pre-
665 existing HPRT mutants. To induce mutation, cells were incubated for 3 hours in serum-
666 free MEM containing 150 µg/mL N-ethyl-N-nitrosourea (ENU) (Sigma). Cells were then

bioRxiv preprint doi: https://doi.org/10.1101/2023.05.07.539748; this version posted May 8, 2023. The copyright holder for this preprint (which was not certified by peer review) is the author/funder, who has granted bioRxiv a license to display the preprint in perpetuity. It is made available under aCC-BY-NC-ND 4.0 International license.

maintained in ENU-free medium for 9 days to allow mutations to establish and existing HPRT to degrade. 1 x 10^6 cells from each cell line were harvested and plated in dialyzed FBS medium containing 5 µg/mL 6-thioguanine (Chem-Impex), in parallel with 1 x 10^6 untreated control cells for each cell line. Cells were plated at a density of 1 x 10^5 cells per 15-cm dish to allow for efficient selection and colony separation, and to prevent potential ”metabolic cooperation“[37]. In tandem, for each cell line 200 cells from untreated and control conditions were plated in triplicate 10-cm dishes in non-selective medium to calculate plating efficiency. After 3 weeks of growth, surviving colonies were fixed and stained with a crystal violet/glutaraldehyde solution as previously described[98]. Colonies were counted, and HPRT mutation rate was calculated as plating-efficiency adjusted number of HPRT-negative colonies containing >50 cells. Appropriate concentrations of ENU and 6-TG, as well as optimal plating densities and growth conditions, were determined prior to the experiment described above through optimization and dose titration experiments.

Digital droplet PCR measurement of CRISPR cleavage rate

A ddPCR assay similar to a previously published method[99] was used for time-course quantification of CRISPR DSB induction across species. qPCR primers at conserved sites flanking the guide RNA target site in the *PTEN* gene were designed such that cleavage would prevent PCR amplification. As an internal copy number reference control, a second set of previously validated qPCR primers targeting an ultraconserved element present in all mammals as a single copy per genome (UCE.359) was designed based on published sequences[100]. To allow for multiplexing and copy number normalization of *PTEN* within each ddPCR reaction, 5‘ fluorescent hydrolysis probes

bioRxiv preprint doi: https://doi.org/10.1101/2023.05.07.539748; this version posted May 8, 2023. The copyright holder for this preprint (which was not certified by peer review) is the author/funder, who has granted bioRxiv a license to display the preprint in perpetuity. It is made available under aCC-BY-NC-ND 4.0 International license.

690 (FAM for *PTEN* and HEX for UCE.359) targeting conserved sequences were designed,
691 with 3‘ Iowa Black® and internal ZEN™ quenchers (Integrated DNA Technologies). All
692 primers and probes were checked for specificity by BLAST against each species’
693 genome.[100] Fibroblasts were transfected with *PTEN* CRISPR RNP as described in
694 “Next-generation sequencing of CRISPR repair products” and returned to cell culture
695 incubators. At the indicated times post-transfection, cells were harvested, flash frozen,
696 and genomic DNA was isolated with the Wizard Genomic DNA Purification Kit
697 (Promega). During isolation, newly lysed cells were treated with Proteinase K and
698 RNase A for 30 minutes each at 37°C to minimize the possibility of residual CRISPR
699 RNP activity. DNA concentration was measured on a Nanodrop spectrophotometer, and
700 genomic DNA was pre-digested with BamHI-HF (NEB) and XhoI (NEB), which do not
701 cut within target amplicons, to maximize PCR efficiency and distribution across droplets.
702 15 ng of genomic DNA per sample was added to duplicate PCR reactions using the
703 ddPCR™ Supermix for Probes (No dUTP) master mix (Bio-Rad). Droplets were
704 prepared and measured according to manufacturer instructions. Briefly, each 20 µL
705 reaction was mixed with 70 µL Droplet Generation Oil for Probes (Bio-Rad) and droplets
706 were formed in a QX100 Droplet Generator (Bio-Rad). 40 µL of droplets per reaction
707 were transferred to 96-well PCR plates and sealed with a PX1 PCR Plate Sealer (Bio-
708 Rad). The sealed plates were then subjected to PCR using a pre-optimized cycling
709 protocol. Following PCR, the plates were loaded into a QX100™ Droplet Reader (Bio-
710 Rad) and each droplet measured on both FAM and HEX channels. *PTEN* copy number
711 normalized to UCE.359 reference copy number within each well was determined with
712 QuantaSoft™ software (Bio-Rad). For each species, positive/negative gates in mock-

bioRxiv preprint doi: https://doi.org/10.1101/2023.05.07.539748; this version posted May 8, 2023. The copyright holder for this preprint (which was not certified by peer review) is the author/funder, who has granted bioRxiv a license to display the preprint in perpetuity. It is made available under aCC-BY-NC-ND 4.0 International license.

transfected control samples were adjusted as necessary to compensate for differences in multiplex PCR efficiency/specificity and "rain" droplets between species and bring normalized *PTEN* copy number closer to 1. The control gates were then applied across all samples/time points within the same species and used for *PTEN* copy number calculation.

Flow cytometric measurement of CRISPR RNP transfection efficiency

CRISPR RNP transfections were performed as described above, but with ATTO-550 fluorescently-labeled tracRNA (Integrated DNA Technologies). At 0h and 24h post-transfection, cells were harvested, pelleted, and analyzed by flow cytometry on a CytoFlex S Flow Cytometer (Beckman Coulter). Gain and ATTO-550 positive gates were set based on mock-transfected control cells included in each experiment.

Senescence-associated β-galactosidase (SA-β-gal) staining

SA-β-gal staining was performed as previously described.[101,102] Cells were washed twice with PBS and fixed in a solution containing 2% formaldehyde and 0.2% glutaraldehyde in PBS for 5 min at room temperature. After fixation, cells were immediately washed twice with PBS and stained in a solution containing 1 mg/mL 5-bromo-4-chloro-3-indolyl P3-D-galactoside (X-Gal), 40 mM citric acid/sodium phosphate buffer, pH 6.0, 5 mM potassium ferrocyanide, 5 mM potassium ferricyanide, 150 mM NaCl, and 2 mM $MgCl_2$. Plates were incubated at 37°C for 16 h without CO_2. Colorimetric images were taken from different areas of each plate and quantified.

Cell survival assay

bioRxiv preprint doi: https://doi.org/10.1101/2023.05.07.539748; this version posted May 8, 2023. The copyright holder for this preprint (which was not certified by peer review) is the author/funder, who has granted bioRxiv a license to display the preprint in perpetuity. It is made available under aCC-BY-NC-ND 4.0 International license.

Percentage of live cells was quantified using the Annexin-V FLUOS Staining Kit (Roche) following the manufacturer's instructions. After staining, cells were analyzed on a CytoFlex S flow cytometer (Beckman Coulter).

p53 activity

To test p53 activity in cultured primary fibroblasts, 150,000 cells were seeded in 6-well plates 1 day before transfection with 1 µg pp53-TA-Luc vector (Clontech) and 0.015 µg pRL-CMV-Renilla (Promega) to normalize for transfection efficiency. Transfections were performed using PEI MAX Transfection Grade Linear Polyethylenimine Hydrochloride (MW 40,000) (Polysciences) according to manufacturer instructions. 24h after transfections cells were lysed using 50µl passive lysis buffer (Promega) per 10^5 cells and flash frozen/thawed two times in liquid nitrogen and a 37°C water bath. Luciferase assays were performed using the Dual-Luciferase Reporter Assay System (Promega) and program DLR-2-INJ on a Glomax 20/20 Luminometer (Promega) with 20µl cell extract as the input.

Generation of NHEJ and HR reporter cell lines

NHEJ and HR reporter constructs[38] were digested with NheI restriction enzyme and purified with the QIAEX II gel extraction kit (QIAGEN). The same plasmid DNA preparation was used for generating all reporter cell lines of the studied species. Cells PD < 15 were recovered from liquid nitrogen and passaged once before the integration of the constructs. 0.25 µg of linearized NHEJ and HR constructs were electroporated into one million cells for each cell line. Two days after transfection, media was refreshed, and G418 was applied to select stable integrant clones. Triplicates of each

bioRxiv preprint doi: https://doi.org/10.1101/2023.05.07.539748; this version posted May 8, 2023. The copyright holder for this preprint (which was not certified by peer review) is the author/funder, who has granted bioRxiv a license to display the preprint in perpetuity. It is made available under aCC-BY-NC-ND 4.0 International license.

reporter in each cell line were prepared to obtain an adequate number of stable clones. Clones from triplicate plates were pooled to get at least 50 clones per reporter per cell line.

DSB repair assays and flow cytometry analysis

DSB repair assays were performed as previously described[103]. Briefly, growing cells were co-transfected with 3 µg of plasmid encoding I-SceI endonuclease and 0.03 µg of plasmid encoding DsRed. The same batch of I-SceI and DsRed mixture was used throughout all species to avoid batch-to-batch variation. To test the effect of CIRBP on DSB repair, 3 µg of CIRBP plasmids were co-transfected with I-SceI and DsRed plasmids. Three days after transfection, the numbers of GFP+ and DsRed+ cells were determined by flow cytometry on a CytoFlex S Flow Cytometer (Beckman Coulter). For gating strategy see Supplementary Figure 4 in Supplementary Information. For each sample, a minimum of 50,000 cells was analyzed. DSB repair efficiency was calculated by dividing the number of GFP+ cells by the number of DsRed+ cells.

For knockdown experiments, bowhead whale cells containing the NHEJ reporter were transfected with 120 pmol of anti-bwCIRBP or control siRNAs (Dharmacon) 3 days before I-Sce1/DsRed transfections using an Amaxa Nucleofector (U-023 program). The efficiency of knockdown was determined by Western blot.

For the extrachromosomal assay and fidelity analysis, NHEJ reporter plasmid was digested with I-Sce1 for 6h and purified using a QIAEX II Gel Extraction Kit (QIAGEN). Exponentially growing cells were transfected using an Amaxa nucleofector with the U-023 program. In a typical reaction, 10^6 cells were transfected with 0.25 µg of

bioRxiv preprint doi: https://doi.org/10.1101/2023.05.07.539748; this version posted May 8, 2023. The copyright holder for this preprint (which was not certified by peer review) is the author/funder, who has granted bioRxiv a license to display the preprint in perpetuity. It is made available under aCC-BY-NC-ND 4.0 International license.

predigested NHEJ reporter substrate along with 0.025 µg of DsRed to serve as a transfection control. 72h after transfection, cells were harvested and analyzed by flow cytometry on a BD LSR II instrument. At least 20,000 cells were collected for each sample. Immediately after FACS, genomic DNA was isolated from cells using the QIAGEN Blood & Tissue kit. DSB repair sites in the NHEJ construct were amplified by PCR using Phusion polymerase (NEB), cloned using the TOPO Blunt cloning kit (NEB), and sent for Sanger sequencing. At least 100 sequenced clones were aligned and analyzed using the ApE software.

Western blotting

All antibodies were checked for conservation of the target epitope in the protein sequence of each included species, and only those targeting regions conserved across these species were used. For a limited number of proteins where the available antibodies with specific epitope information disclosed did not target conserved regions, we selected antibodies based on demonstrated reactivity across a broad range of mammal species and always confirmed these results with multiple antibodies. Information on antibodies is provided in Supplementary Methods.

Exponentially growing cells were harvested with trypsin and counted, and 10^6 cells were resuspended in 100 µL of PBS containing protease inhibitors. 100µL of 2x Laemmli buffer (Bio-Rad) was added, and samples were boiled at 95ºC for 10 minutes. Samples were separated with 4-20% gradient SDS-PAGE, transferred to a PVDF membrane, and blocked in 5% milk-TBS-T for 2 hours at room temperature. Membranes were incubated overnight at +4ºC with primary antibodies in 5% milk-TBS-T. After 3 washes for 10 minutes with TBS-T, membranes were incubated for 1 hour at room temperature

bioRxiv preprint doi: https://doi.org/10.1101/2023.05.07.539748; this version posted May 8, 2023. The copyright holder for this preprint (which was not certified by peer review) is the author/funder, who has granted bioRxiv a license to display the preprint in perpetuity. It is made available under aCC-BY-NC-ND 4.0 International license.

with secondary antibodies conjugated with HRP or a fluorophore. After 3 washes with TBS-T signal was developed for HRP secondaries with Clarity Western ECL Substrate (Bio-Rad). CIRBP and RPA2 expression were each measured with 3 different antibodies targeting conserved epitopes (Extended Data Figure 7c, d).

PARP activity

PARP activity was measured in cell nuclear extracts with the PARP Universal Colorimetric Assay Kit (Trevigen) according to the manufacturer's instructions. Nuclear extracts were prepared using EpiQuik Nuclear Extraction Kit (EpigenTek) following manufacturer protocol. 2.5µg of total nuclear extract was added to measure PARP activity.

For measurement of PARylation efficiency, cells were treated with 400µM H_2O_2 for 15 and 30 min. At the end of incubation, cells were placed on ice, washed once with PBS, and lysed directly on a plate with 2x Laemmli buffer. Samples were boiled for 10min at 95ºC and processed by Western Blot.

Pulsed-field gel electrophoresis and analysis of DSBs

After irradiation and repair incubation, confluent human and bowhead whale skin fibroblasts were harvested, ~400,000 cells were resuspended in PBS, mixed with an equal volume of 1.4% low gelling temperature agarose and embedded into agarose plugs. Plugs were kept for 1h at +4ºC and incubated in lysis solution 1 (0.5M EDTA, 2% sodium sarcosine, 0.5 mg/ml Proteinase K) for 24h at +4ºC. Subsequently plugs were placed into lysis solution 2 (1.85M NaCl, 0.15M KCl, 5mM $MgCl_2$, 2mM EDTA, 4mM Tris pH 7.5, 0.5% TritonX100) for 40h at +4ºC. Plugs were then washed two times for 1h in

bioRxiv preprint doi: https://doi.org/10.1101/2023.05.07.539748; this version posted May 8, 2023. The copyright holder for this preprint (which was not certified by peer review) is the author/funder, who has granted bioRxiv a license to display the preprint in perpetuity. It is made available under aCC-BY-NC-ND 4.0 International license.

TE buffer and stored in TE buffer at +4ºC. PFGE was carried out with a CHEF DRII system (Bio-Rad) in 0.8% agarose gels. The gels were run at 14°C with linearly increasing pulse times from 50 to 5,000 s for 66 h at a field strength of 1.5 V/cm. Gels were stained with 0.5mg/ml ethidium bromide for 4h, washed with TBE buffer and imaged. Quantitative analysis was performed with Image Lab software (Bio-Rad). The fraction of DNA entering the gel was quantified. Samples irradiated with various doses and not incubated for repair served as a calibration to determine the percentage of remaining DSBs in the repair samples from the fraction of DNA entering the gel.

Construction of lentiviral overexpression vectors and lentivirus production

The coding sequence of bwCIRBP was amplified by PCR using Phusion polymerase (NEB), digested with EcoRI and NotI, and cloned in between EcoRI and NotI sites of the Lego-iC2 plasmid. The sequence was verified by Sanger sequencing.

Lentiviral particles were produced in Lenti-X 293T cells (Takara). Approximately $10x10^6$ cells were transfected with a mixture of pVSV-G (1.7 µg), psPAX2 (3.4 µg) and Lego-iC2-bwCIRBP (6.8 µg) using PEI MAX (Polysciences). The day after transfection, DMEM culture medium (ThermoFisher) was replaced with fresh medium and lentiviral particles were harvested from the supernatant for the next 3 days.

Quantification of micronuclei

Two different approaches were used. To analyze binucleated cells containing micronuclei (MN), 20,000 cells were plated per chamber slide 2d before ionizing radiation. Immediately after irradiation (for human cells) or 2d after irradiation (for bowhead whale cells), cytochalasin B was added to cell culture media at a final

bioRxiv preprint doi: https://doi.org/10.1101/2023.05.07.539748; this version posted May 8, 2023. The copyright holder for this preprint (which was not certified by peer review) is the author/funder, who has granted bioRxiv a license to display the preprint in perpetuity. It is made available under aCC-BY-NC-ND 4.0 International license.

concentration 0.5 μg/ml, and cells were incubated for an additional 72h. At the end of incubation, cells were washed with PBS, incubated in 75mM KCl for 10min at RT, fixed with ice-cold methanol for 1.5 min, air-dried, and stored. Immediately before the analysis, cells were stained with 100 μg/ml acridine orange for 2min, washed with PBS, mounted in PBS and analyzed by fluorescence microscopy. At least 1000 binucleated cells were analyzed per sample.

For analysis of MN in single cells overexpressing bwCIRBP, exponentially growing cells were transduced with LEGO-iC2-bwCIRBP lentivirus in the presence of 10 μg/ml polybrene. Two days after transduction, cells were passaged, and irradiated the following day. 3 days after irradiation, cells were fixed with 2% formaldehyde for 15 min, washed with PBS, permeabilized with 0.2% TritonX100 for 2min, washed in PBS, and mounted in VECTASHIELD Antifade Mounting Medium with DAPI. Cells were analyzed with a fluorescent microscope. At least 1000 cells were analyzed per condition.

Host cell reactivation assay

A host cell reactivation assay was used to measure the repair of UV-induced DNA damage through nucleotide excision repair as previously described.[33]

To measure the repair of oxidative DNA damage (base excision repair), 20 μg of firefly luciferase (FFL) plasmid was mixed with 20-200 μM methylene blue (MB), and water was added to a final volume of 0.4ml. DNA-MB mixture was dropped onto a petri dish and placed on ice. An additional petri dish containing water was placed on top. The DNA-MB mixture was exposed to visible light for 15 min using a 100W lamp at an 11cm

bioRxiv preprint doi: https://doi.org/10.1101/2023.05.07.539748; this version posted May 8, 2023. The copyright holder for this preprint (which was not certified by peer review) is the author/funder, who has granted bioRxiv a license to display the preprint in perpetuity. It is made available under aCC-BY-NC-ND 4.0 International license.

distance. Damaged DNA was purified, and the host cell reactivation assay was performed as described for UV-induced DNA damage.

Cyclobutane pyrimidine dimer (CPD) ELISA

Human and bowhead whale skin fibroblasts were grown until they reached confluency before UVC radiation. Cells were irradiated in PBS at doses of 0, 5, 10, 20 and 30J/m^2 and harvested immediately for building an induction curve. To assess DNA repair, cells were irradiated at 30 J/m^2 and incubated for 6, 24 and 48h before harvesting. Genomic DNA was isolated using QIAamp Blood Kit (Qiagen). Samples of DNA were diluted in PBS to a final concentration of 2 µg/ml, denatured at 100ºC for 10min and incubated in an ice bath for 15 min. 100 ng of denatured DNA solution was applied to ELISA plate wells precoated with protamine sulfate (Cosmo Bio) and dried O/N at 37ºC. Plates were washed five times with PBS supplemented with 0.05% Tween-20 (PBS-T) and blocked in 2% FBS in PBS-T for 30min at 37ºC. After 5 washes with PBS-T, plates were incubated with mouse monoclonal anti-CPD antibodies (Clone TDM-2, 1:1000) in PBS for 30 min at 37ºC. Plates were then sequentially incubated with goat-anti mouse biotin IgG (Invitrogen, 1:1000) and streptavidin-HRP (Invitrogen, 1:5000) in PBS for 30 min at 37ºC each with 5 washes with PBS-T before and after incubations. Plates were washed with citrate buffer and incubated with substrate solution (citrate buffer/o-phenylenediamine/hydrogen peroxide) for 30 min at 37ºC. Finally, the reaction was stopped with 2M H_2SO_4 and the absorbance was measured at 492 nm with a plate reader.

CIRBP variant sequence analysis

bioRxiv preprint doi: https://doi.org/10.1101/2023.05.07.539748; this version posted May 8, 2023. The copyright holder for this preprint (which was not certified by peer review) is the author/funder, who has granted bioRxiv a license to display the preprint in perpetuity. It is made available under aCC-BY-NC-ND 4.0 International license.

Identification of rare codons (<10% usage for the corresponding amino acid in human CDS sequences) was performed on CIRBP coding sequences using the Benchling Codon Optimization Tool.[104] Codon adaptation index (CAI) was calculated with human codon frequencies using the E-CAI web server.[53]

RNA isolation and RNA-seq analysis

RNA from exponentially growing or senescent human and bowhead whale primary skin fibroblasts was isolated using the Quick-RNA MiniPrep kit (Zymo Research) according to manufacturer instructions.

The RNA-seq reads were first processed using Trim_Galore (version 0.6.6). Cleaned RNA-seq reads were used to quantify gene expression with Salmon (version 1.4.0).[105] Transcript FASTA files of species were from our published de novo transcriptome assemblies.[106] Transcript FASTA files were indexed with the command “Salmon index” with default parameters. Cleaned RNA-seq reads were aligned to the indexed transcript with the specific parameters (--useVBOpt --seqBias --gcBias), which were set for sequence-specific bias correction and fragment GC bias correction. The read counts of genes obtained from Salmon were further normalized by trimmed mean of M-values (TMM)[107] and median of ratios methods.[108]

LC-MS proteomic analysis of fibroblasts

2 15-cm dishes of growing primary fibroblasts from 2 cell lines for each species were harvested for protein. Cells were washed with PBS and pellets were snap frozen and stored in liquid nitrogen until processing. Cells were solubilized with 5% SDS; 50 mM TEAB pH 7, and sonicated at 8°C with 10x 45s pulses using 30% power with 15 s rest

bioRxiv preprint doi: https://doi.org/10.1101/2023.05.07.539748; this version posted May 8, 2023. The copyright holder for this preprint (which was not certified by peer review) is the author/funder, who has granted bioRxiv a license to display the preprint in perpetuity. It is made available under aCC-BY-NC-ND 4.0 International license.

910 between each pulse with a cup horn Q800R3 Sonicator System (Qsonica; Newtown
911 CT). Soluble proteins were reduced with 10 mM DTT for 30 min at 55°C, followed by
912 alkylation with 15 mM iodoacetamide at 25°C in the dark for 30 min. S-trap micro
913 columns (Protifi; Farmingdale, NY) were employed after this step for overnight tryptic
914 digestion and peptide isolation according to manufacturer instructions. All solvents were
915 MS-grade. Resulting tryptic peptides were resuspended in MS-grade water and were
916 quantified using a Pierce™ Quantitative Fluorometric Peptide Assay (Thermo Fisher cat
917 #23290). Prior to MS, peptides were mixed with a common internal retention time
918 standards[109] (CiRT) peptide mix (50 fmol CiRT/2ug total tryptic peptides) and
919 acetonitrile (ACN) and formic acid were added to concentrations of 5% and 0.2%
920 respectively. The final concentration of the peptide mix was 0.5µg/µl. 2ug (4ul) of each
921 were resolved by nano-electrospray ionization on an Orbitrap Fusion Lumos MS
922 instrument (Thermo) in positive ion mode. A 30 cm home-made column packed with 1.8
923 µm C-18 beads was employed to resolve the peptides. Solvent A was 0.1% formic acid
924 and solvent B was 80% acetonitrile with 0.1% formic acid and flow rate was 300 nl/min.
925 The length of the run was 3 h with a 155 min gradient from 10-38% B. HCD (30%
926 collision energy) was used for MS2 fragmentation and dynamic exclusion was operative
927 after a single time and lasted for 30s. Other details of the run parameters may be found
928 in the embedded run report of the RAW data file uploaded to the ProteomeXchange
929 database. Peptide assignments and quantitation were done using the label-free quant
930 match between runs (LFQ-MBR) workflow of MSFragger[110–112]. MaxLFQ with a
931 minimum of two ions was implemented and normalization was selected. Additional
932 details are available in MSFragger log files. Searches were performed within the

bioRxiv preprint doi: https://doi.org/10.1101/2023.05.07.539748; this version posted May 8, 2023. The copyright holder for this preprint (which was not certified by peer review) is the author/funder, who has granted bioRxiv a license to display the preprint in perpetuity. It is made available under aCC-BY-NC-ND 4.0 International license.

Philosopher/Fragpipe pipeline that incorporates PeptideProphet and ProteinProphet filtering steps to increase the likelihood of correct assignments.[113] The databases used for searches were predicted proteins from the published bowhead genome[114] as well as our custom proteome derived from our de novo sequenced and Trinity[115,116]-assembled pool of transcriptomes from whale tissues. Human (UP000005640), mouse (UP000000589), and bovine (UP000009136) databases were from the latest build available from Uniprot.[117] For the searches, databases also included a reverse complement form of all peptides as well as common contaminants to serve as decoys for false discovery rate (FDR) calculation by the target/decoy approach (decoy present at 50%).[118] Final FDR was below 1%.

Statistical analyses

Statistical comparisons were performed as indicated in the figure legends. Unless otherwise specified in the text or legend, *n* refers to separate biological replicate cell lines, isolated from different individuals for a given species. Exceptions include specific genetically modified cell lines or clones, e.g. tumor suppressor knockout lines and Ku-deficient MEFs. In such cases, *n* refers to technical replicates and indicates the number of times the experiment was repeated with the specified cell line. Details for comparisons done by ANOVA are included in Supplementary Information.

Data Availability

Proteomics data are accessible through ProteomeXchange [URL to be added]. DNA sequence (CRISPR repair fidelity analysis) and RNA sequence (transcriptome) data are accessible through NCBI Sequence Read Archive (SRA) [URL to be added].

bioRxiv preprint doi: https://doi.org/10.1101/2023.05.07.539748; this version posted May 8, 2023. The copyright holder for this preprint (which was not certified by peer review) is the author/funder, who has granted bioRxiv a license to display the preprint in perpetuity. It is made available under aCC-BY-NC-ND 4.0 International license.

References

1. Tacutu, R. *et al.* Human Ageing Genomic Resources: new and updated databases. *Nucleic Acids Res* **46**, D1083–D1090 (2018).

2. Peto, R. Epidemiology, multistage models, and short-term mutagenicity tests. in *The origins of human cancer* (eds. Hiatt, H., Watson, J. & Winsten, J.) vol. 4 1403–1428 (Cold Spring Harbor Conferences on Cell Proliferation, 1977).

3. Abegglen, L. M. *et al.* Potential Mechanisms for Cancer Resistance in Elephants and Comparative Cellular Response to DNA Damage in Humans. *JAMA* **314**, 1850 (2015).

4. Vazquez, J. M., Sulak, M., Chigurupati, S. & Lynch, V. J. A Zombie LIF Gene in Elephants Is Upregulated by TP53 to Induce Apoptosis in Response to DNA Damage. *Cell Rep* **24**, 1765–1776 (2018).

5. Sulak, M. *et al.* TP53 copy number expansion is associated with the evolution of increased body size and an enhanced DNA damage response in elephants. *Elife* **5**, (2016).

6. TEK & Bowhead Life History and Longevity - The North Slope Borough. https://www.north-slope.org/departments/wildlife-management/studies-research-projects/bowhead-whales/traditional-ecological-knowledge-of-bowhead-whales/tek-bowhead-life-history-and-longevity/.

7. George, J. C. & Bockstoce, J. R. Two historical weapon fragments as an aid to estimating the longevity and movements of bowhead whales. *Polar Biol* **31**, 751–754 (2008).

8. Rosa, C. *et al.* Age estimates based on aspartic acid racemization for bowhead whales (Balaena mysticetus) harvested in 1998-2000 and the relationship between racemization rate and body temperature. *Mar Mamm Sci* **29**, 424–445 (2013).

9. Philo, L. M., Shotts, E. B. & George, J. C. Morbidity and mortality- The bowhead whale. *Soc. Mar. Mammal., Spec. Publ* 275–312 (1993).

10. George, J. C. *et al.* Age and growth estimates of bowhead whales (Balaena mysticetus) via aspartic acid racemization. *Can J Zool* **77**, 571–580 (1999).

11. Wetzel, D. *et al.* Age estimation for bowhead whales, Balaena mysticetus, using aspartic acid racemization with enhanced hydrolysis and derivatization procedures. *Paper SC/65b/BRG05 presented to the Scientific Committee of the International Whaling Commission* (2014).

12. George, J. C. *et al.* A new way to estimate the age of bowhead whales (Balaena mysticetus) using ovarian corpora counts. *https://doi.org/10.1139/z11-057* **89**, 840–852 (2011).

13. Boddy, A. M. *et al.* Lifetime cancer prevalence and life history traits in mammals. *Evol Med Public Health* **2020**, 187–195 (2020).

14. Vincze, O. *et al.* Cancer risk across mammals. *Nature* **601**, 263–267 (2022).

15. Tollis, M., Boddy, A. M. & Maley, C. C. Peto's Paradox: how has evolution solved the problem of cancer prevention? *BMC Biol* **15**, (2017).

bioRxiv preprint doi: https://doi.org/10.1101/2023.05.07.539748; this version posted May 8, 2023. The copyright holder for this preprint (which was not certified by peer review) is the author/funder, who has granted bioRxiv a license to display the preprint in perpetuity. It is made available under aCC-BY-NC-ND 4.0 International license.

16. Keane, M. *et al.* Insights into the evolution of longevity from the bowhead whale genome. *Cell Rep* **10**, 112–122 (2015).

17. Tollis, M. *et al.* Return to the Sea, Get Huge, Beat Cancer: An Analysis of Cetacean Genomes Including an Assembly for the Humpback Whale (Megaptera novaeangliae). *Mol Biol Evol* **36**, 1746–1763 (2019).

18. Seim, I. *et al.* The transcriptome of the bowhead whale Balaena mysticetus reveals adaptations of the longest-lived mammal. *Aging* **6**, 879–899 (2014).

19. Armitage, P. & Doll, R. The age distribution of cancer and a multi-stage theory of carcinogenesis. *Br J Cancer* **8**, 1–12 (1954).

20. Rangarajan, A., Hong, S. J., Gifford, A. & Weinberg, R. A. Species- and cell type-specific requirements for cellular transformation. *Cancer Cell* **6**, 171–183 (2004).

21. Vazquez, J. M., Sulak, M., Chigurupati, S. & Lynch, V. J. A Zombie LIF Gene in Elephants Is Upregulated by TP53 to Induce Apoptosis in Response to DNA Damage. *Cell Rep* **24**, 1765–1776 (2018).

22. Vazquez, J. M. & Lynch, V. J. Pervasive duplication of tumor suppressors in Afrotherians during the evolution of large bodies and reduced cancer risk. *Elife* **10**, 1–45 (2021).

23. Vazquez, J. M. *et al.* Parallel evolution of reduced cancer risk and tumor suppressor duplications in Xenarthra. *Elife* **11**, (2022).

24. Boveri, T. Concerning the origin of malignant tumours by Theodor Boveri. Translated and annotated by Henry Harris. *J Cell Sci* **121**, 1–84 (2008).

25. Hasty, P., Campisi, J., Hoeijmakers, J., van Steeg, H. & Vijg, J. *Aging and Genome Maintenance: Lessons from the Mouse?* http://science.sciencemag.org/.

26. Kashiyama, K. *et al.* Malfunction of nuclease ERCC1-XPF results in diverse clinical manifestations and causes Cockayne syndrome, xeroderma pigmentosum, and Fanconi anemia. *Am J Hum Genet* **92**, 807–819 (2013).

27. Navarro, C. L., Cau, P. & Lévy, N. Molecular bases of progeroid syndromes. *Human Molecular Genetics* vol. 15 R151–R161 Preprint at https://doi.org/10.1093/hmg/ddl214 (2006).

28. Varon, R. *et al.* Nibrin, a novel DNA double-strand break repair protein, is mutated in Nijmegen breakage syndrome. *Cell* **93**, 467–476 (1998).

29. Liu, B. *et al.* Genomic instability in laminopathy-based premature aging. *Nat Med* **11**, 780–785 (2005).

30. Lorenzini, A. *et al.* Significant Correlation of Species Longevity with DNA Double Strand Break-Recognition but not with Telomere Length. *Mech Ageing Dev* **130**, 784 (2009).

31. Zhang, L. *et al.* Maintenance of genome sequence integrity in long- And short-lived rodent species. *Sci Adv* **7**, (2021).

bioRxiv preprint doi: https://doi.org/10.1101/2023.05.07.539748; this version posted May 8, 2023. The copyright holder for this preprint (which was not certified by peer review) is the author/funder, who has granted bioRxiv a license to display the preprint in perpetuity. It is made available under aCC-BY-NC-ND 4.0 International license.

32. Cagan, A. *et al.* Somatic mutation rates scale with lifespan across mammals. *Nature 2022* 1–8 (2022) doi:10.1038/s41586-022-04618-z.

33. Tian, X. *et al.* SIRT6 Is Responsible for More Efficient DNA Double-Strand Break Repair in Long-Lived Species. *Cell* **177**, 622-638.e22 (2019).

34. Fortunato, A., Fleming, A., Aktipis, A. & Maley, C. C. Upregulation of DNA repair genes and cell extrusion underpin the remarkable radiation resistance of Trichoplax adhaerens. *PLoS Biol* **19**, (2021).

35. Tian, X. *et al.* Evolution of telomere maintenance and tumour suppressor mechanisms across mammals. *Philosophical Transactions of the Royal Society B: Biological Sciences* **373**, (2018).

36. Borowicz, S. *et al.* The soft agar colony formation assay. *J Vis Exp* e51998 (2014) doi:10.3791/51998.

37. Johnson, G. E. Mammalian Cell HPRT Gene Mutation Assay: Test Methods. in 55–67 (2012). doi:10.1007/978-1-61779-421-6_4.

38. Seluanov, A., Mao, Z. & Gorbunova, V. Analysis of DNA Double-strand Break (DSB) Repair in Mammalian Cells. *J Vis Exp* 43 (2010) doi:10.3791/2002.

39. Guo, T. *et al.* Harnessing accurate non-homologous end joining for efficient precise deletion in CRISPR/Cas9-mediated genome editing. *Genome Biol* **19**, (2018).

40. Richardson, C. D., Ray, G. J., Bray, N. L. & Corn, J. E. Non-homologous DNA increases gene disruption efficiency by altering DNA repair outcomes. *Nature Communications 2016 7:1* **7**, 1–7 (2016).

41. Chen, J. K., Lin, W. L., Chen, Z. & Liu, H. wen. PARP-1–dependent recruitment of cold-inducible RNA-binding protein promotes double-strand break repair and genome stability. *Proc Natl Acad Sci U S A* **115**, E1759–E1768 (2018).

42. Nishiyama, H. *et al.* A glycine-rich RNA-binding protein mediating cold-inducible suppression of mammalian cell growth. *J Cell Biol* **137**, 899–908 (1997).

43. Sheikh, M. S. *et al.* Identification of several human homologs of hamster DNA damage-inducible transcripts. Cloning and characterization of a novel UV-inducible cDNA that codes for a putative RNA-binding protein. *J Biol Chem* **272**, 26720–26726 (1997).

44. Wellmann, S. *et al.* Oxygen-regulated expression of the RNA-binding proteins RBM3 and CIRP by a HIF-1-independent mechanism. *J Cell Sci* **117**, 1785–1794 (2004).

45. Yang, C. & Carrier, F. The UV-inducible RNA-binding protein A18 (A18 hnRNP) plays a protective role in the genotoxic stress response. *J Biol Chem* **276**, 47277–47284 (2001).

46. Yang, R., Weber, D. J. & Carrier, F. Post-transcriptional regulation of thioredoxin by the stress inducible heterogenous ribonucleoprotein A18. *Nucleic Acids Res* **34**, 1224–1236 (2006).

bioRxiv preprint doi: https://doi.org/10.1101/2023.05.07.539748; this version posted May 8, 2023. The copyright holder for this preprint (which was not certified by peer review) is the author/funder, who has granted bioRxiv a license to display the preprint in perpetuity. It is made available under aCC-BY-NC-ND 4.0 International license.

47. Yang, R. *et al.* Functional significance for a heterogenous ribonucleoprotein A18 signature RNA motif in the 3'-untranslated region of ataxia telangiectasia mutated and Rad3-related (ATR) transcript. *J Biol Chem* **285**, 8887–8893 (2010).

48. Roilo, M., Kullmann, M. K. & Hengst, L. Cold-inducible RNA-binding protein (CIRP) induces translation of the cell-cycle inhibitor p27Kip1. *Nucleic Acids Res* **46**, 3198–3210 (2018).

49. Elsner, R., Meiselman, H. J. & Baskurt, O. K. TEMPERATURE-VISCOSITY RELATIONS OF BOWHEAD WHALE BLOOD: A POSSIBLE MECHANISM FOR MAINTAINING COLD BLOOD FLOW. *Mar Mamm Sci* **20**, 339–344 (2004).

50. George, J. C. Growth, morphology and energetics of bowhead whales (Balaena mysticetus). (University of Alaska Fairbanks, 2009).

51. Gotic, I. *et al.* Temperature regulates splicing efficiency of the cold-inducible RNA-binding protein gene Cirbp. *Genes Dev* **30**, 2005–2017 (2016).

52. Al-Fageeh, M. B. & Smales, C. M. Cold-inducible RNA binding protein (CIRP) expression is modulated by alternative mRNAs. *RNA* **15**, 1165–1176 (2009).

53. Puigbò, P., Bravo, I. G. & Garcia-Vallvé, S. E-CAI: a novel server to estimate an expected value of Codon Adaptation Index (eCAI). *BMC Bioinformatics* **9**, (2008).

54. Zou, Y., Liu, Y., Wu, X. & Shell, S. M. Functions of Human Replication Protein A (RPA): From DNA Replication to DNA Damage and Stress Responses. *J Cell Physiol* **208**, 267 (2006).

55. Wold, M. S. Replication protein A: a heterotrimeric, single-stranded DNA-binding protein required for eukaryotic DNA metabolism. *Annu Rev Biochem* **66**, 61–92 (1997).

56. Paulsen, R. D. *et al.* A genome-wide siRNA screen reveals diverse cellular processes and pathways that mediate genome stability. *Mol Cell* **35**, 228–239 (2009).

57. Toledo, L. I. *et al.* ATR prohibits replication catastrophe by preventing global exhaustion of RPA. *Cell* **155**, 1088 (2013).

58. Velegzhaninov, I. O. *et al.* Radioresistance, DNA Damage and DNA Repair in Cells With Moderate Overexpression of RPA1. *Front Genet* **11**, 855 (2020).

59. Guven, M., Brem, R., Macpherson, P., Peacock, M. & Karran, P. Oxidative damage to RPA limits the nucleotide excision repair capacity of human cells. *J Invest Dermatol* **135**, 2834 (2015).

60. Graziano, S. *et al.* Lamin A/C recruits ssDNA protective proteins RPA and RAD51 to stalled replication forks to maintain fork stability. *Journal of Biological Chemistry* **297**, 101301 (2021).

61. Perrault, R., Cheong, N., Wang, H., Wang, H. & Iliakis, G. RPA facilitates rejoining of DNA double-strand breaks in an in vitro assay utilizing genomic DNA as substrate. *int. j. radiat. biol* **77**, 593–607 (2001).

62. Krasner, D. S., Daley, J. M., Sung, P. & Niu, H. Interplay between Ku and Replication Protein A in the Restriction of Exo1-mediated DNA Break End Resection. *J Biol Chem* **290**, 18806–18816 (2015).

bioRxiv preprint doi: https://doi.org/10.1101/2023.05.07.539748; this version posted May 8, 2023. The copyright holder for this preprint (which was not certified by peer review) is the author/funder, who has granted bioRxiv a license to display the preprint in perpetuity. It is made available under aCC-BY-NC-ND 4.0 International license.

63. Chen, H., Lisby, M. & Symington, L. S. RPA coordinates DNA end resection and prevents formation of DNA hairpins. *Mol Cell* **50**, 589–600 (2013).

64. Deng, S. K., Gibb, B., de Almeida, M. J., Greene, E. C. & Symington, L. S. RPA Antagonizes Microhomology-Mediated Repair of DNA Double-Strand Breaks. *Nat Struct Mol Biol* **21**, 405 (2014).

65. Guven, M., Brem, R., Macpherson, P., Peacock, M. & Karran, P. Oxidative damage to RPA limits the nucleotide excision repair capacity of human cells. *J Invest Dermatol* **135**, 2834 (2015).

66. Kim, K. *et al.* Novel Checkpoint Response to Genotoxic Stress Mediated by Nucleolin-Replication Protein A Complex Formation. *Mol Cell Biol* **25**, 2463 (2005).

67. Bélanger, F. *et al.* Mutations in Replicative Stress Response Pathways Are Associated with S Phase-specific Defects in Nucleotide Excision Repair *. (2015) doi:10.1074/jbc.M115.685883.

68. Shuck, S. C. & Turchi, J. J. Targeted inhibition of RPA reveals cytotoxic activity, synergy with chemotherapeutic DNA damaging agents and insight into cellular function. *Cancer Res* **70**, 3189 (2010).

69. White, R. R. *et al.* Double-Strand Break Repair by Interchromosomal Recombination: An In Vivo Repair Mechanism Utilized by Multiple Somatic Tissues in Mammals. *PLoS One* **8**, 84379 (2013).

70. Seluanov, A. *et al.* Telomerase activity coevolves with body mass not lifespan. *Aging Cell* **6**, 45–52 (2007).

71. Vazquez, J. M., Kraft, M. & Lynch, V. J. A CDKN2C retroduplication in Bowhead whales is associated with the evolution of extremely long lifespans and alerted cell cycle dynamics. *bioRxiv* 2022.09.07.506958 (2022) doi:10.1101/2022.09.07.506958.

72. Coppé, J. P., Desprez, P. Y., Krtolica, A. & Campisi, J. The Senescence-Associated Secretory Phenotype: The Dark Side of Tumor Suppression. *Annu Rev Pathol* **5**, 99 (2010).

73. Mendiratta, G. *et al.* Cancer gene mutation frequencies for the U.S. population. *Nature Communications 2021 12:1* **12**, 1–11 (2021).

74. Wright, K. M. & Deshmukh, M. Restricting Apoptosis for Postmitotic Cell Survival and its Relevance to Cancer. *http://dx.doi.org/10.4161/cc.5.15.3129* **5**, 1616–1620 (2006).

75. Lieber, M. R., Gu, J., Lu, H., Shimazaki, N. & Tsai, A. G. Nonhomologous DNA end joining (NHEJ) and chromosomal translocations in humans. *Subcell Biochem* **50**, 279–296 (2014).

76. Yoshioka, K. I., Kusumoto-Matsuo, R., Matsuno, Y. & Ishiai, M. Genomic Instability and Cancer Risk Associated with Erroneous DNA Repair. *International Journal of Molecular Sciences 2021, Vol. 22, Page 12254* **22**, 12254 (2021).

77. Yokoyama, A. *et al.* Age-related remodelling of oesophageal epithelia by mutated cancer drivers. *Nature* **565**, 312–317 (2019).

78. Martincorena, I. *et al.* Somatic mutant clones colonize the human esophagus with age. *Science* **362**, 911–917 (2018).

bioRxiv preprint doi: https://doi.org/10.1101/2023.05.07.539748; this version posted May 8, 2023. The copyright holder for this preprint (which was not certified by peer review) is the author/funder, who has granted bioRxiv a license to display the preprint in perpetuity. It is made available under aCC-BY-NC-ND 4.0 International license.

79. Jaiswal, S. *et al.* Age-related clonal hematopoiesis associated with adverse outcomes. *N Engl J Med* **371**, 2488–2498 (2014).

80. Martincorena, I. *et al.* High burden and pervasive positive selection of somatic mutations in normal human skin. *Science (1979)* **348**, 880–886 (2015).

81. Mitchell, E. *et al.* Clonal dynamics of haematopoiesis across the human lifespan. *Nature 2022 606:7913* **606**, 343–350 (2022).

82. Kolora, S. R. R. *et al.* Origins and evolution of extreme life span in Pacific Ocean rockfishes. *Science* **374**, 842–847 (2021).

83. Allen, K. N. & Vázquez-Medina, J. P. Natural Tolerance to Ischemia and Hypoxemia in Diving Mammals: A Review. *Front Physiol* **10**, 1199 (2019).

84. Lombardi, G., Ziemann, E. & Banfi, G. Whole-Body Cryotherapy in Athletes: From Therapy to Stimulation. An Updated Review of the Literature. *Front Physiol* **8**, 258 (2017).

85. Gocoł, R. *et al.* The Role of Deep Hypothermia in Cardiac Surgery. *Int J Environ Res Public Health* **18**, (2021).

86. Liu, Y. *et al.* Chronic hypoxia–induced Cirbp hypermethylation attenuates hypothermic cardioprotection via down-regulation of ubiquinone biosynthesis. *Sci Transl Med* **11**, (2019).

87. Wu, L. *et al.* Therapeutic Hypothermia Enhances Cold-Inducible RNA-Binding Protein Expression and Inhibits Mitochondrial Apoptosis in a Rat Model of Cardiac Arrest. *Mol Neurobiol* **54**, 2697–2705 (2017).

88. Yu, L., Gu, T., Liu, Y., Jiang, X. & Shi, E. Cold-inducible ribonucleic acid-binding protein attenuates acute kidney injuries after deep hypothermic circulatory arrest in rats. *Interact Cardiovasc Thorac Surg* **26**, 124–130 (2018).

89. Li, Y. *et al.* Cold-inducible RNA-binding protein maintains intestinal barrier during deep hypothermic circulatory arrest. *Interact Cardiovasc Thorac Surg* **29**, 583–591 (2019).

90. Pan, H. Z. *et al.* Cold-inducible RNA binding protein agonist enhances the cardioprotective effect of UW solution during extended heart preservation. *Artif Organs* **44**, E406–E418 (2020).

91. Chen, Y. *et al.* Fight to the bitter end: DNA repair and aging. *Ageing Res Rev* **64**, 101154 (2020).

92. Seluanov, A., Vaidya, A. & Gorbunova, V. Establishing Primary Adult Fibroblast Cultures From Rodents. *J Vis Exp* **44**, (2010).

93. Quail, M. A. *et al.* Optimal enzymes for amplifying sequencing libraries. *Nat Methods* **9**, 10–11 (2012).

94. Blackburn, M. C. Development of new tools and applications for high-throughput sequencing of microbiomes in environmental or clinical samples. (2010).

95. Clement, K. *et al.* CRISPResso2 provides accurate and rapid genome editing sequence analysis. *Nature Biotechnology 2019 37:3* **37**, 224–226 (2019).

bioRxiv preprint doi: https://doi.org/10.1101/2023.05.07.539748; this version posted May 8, 2023. The copyright holder for this preprint (which was not certified by peer review) is the author/funder, who has granted bioRxiv a license to display the preprint in perpetuity. It is made available under aCC-BY-NC-ND 4.0 International license.

96. Lee, H. J., Chang, H. Y., Cho, S. W. & Ji, H. P. CRISPRpic: fast and precise analysis for CRISPR-induced mutations via prefixed index counting. *NAR Genom Bioinform* **2**, (2020).

97. GitHub - jstjohn/SeqPrep: Tool for stripping adaptors and/or merging paired reads with overlap into single reads. https://github.com/jstjohn/SeqPrep.

98. Franken, N. A. P., Rodermond, H. M., Stap, J., Haveman, J. & van Bree, C. Clonogenic assay of cells in vitro. *Nat Protoc* **1**, 2315–2319 (2006).

99. Rose, J. C. *et al.* Rapidly inducible Cas9 and DSB-ddPCR to probe editing kinetics. *Nat Methods* **14**, 891 (2017).

100. Hudon, S. F. *et al.* Primers to highly conserved elements optimized for qPCR-based telomere length measurement in vertebrates. *Mol Ecol Resour* **21**, 59–67 (2021).

101. Dimri, G. P. *et al.* A biomarker that identifies senescent human cells in culture and in aging skin in vivo. *Proc Natl Acad Sci U S A* **92**, 9363 (1995).

102. Debacq-Chainiaux, F., Erusalimsky, J. D., Campisi, J. & Toussaint, O. Protocols to detect senescence-associated beta-galactosidase (SA-βgal) activity, a biomarker of senescent cells in culture and in vivo. *Nature Protocols 2009 4:12* **4**, 1798–1806 (2009).

103. Mao, Z. *et al.* SIRT6 promotes DNA repair under stress by activating PARP1. *Science (1979)* **332**, 1443–1446 (2011).

104. Benchling. https://www.benchling.com/.

105. Patro, R., Duggal, G., Love, M. I., Irizarry, R. A. & Kingsford, C. Salmon provides fast and bias-aware quantification of transcript expression. *Nature Methods 2017 14:4* **14**, 417–419 (2017).

106. Lu, J. Y. *et al.* Comparative transcriptomics reveals circadian and pluripotency networks as two pillars of longevity regulation. *Cell Metab* **34**, 836-856.e5 (2022).

107. Robinson, M. D., McCarthy, D. J. & Smyth, G. K. edgeR: a Bioconductor package for differential expression analysis of digital gene expression data. *Bioinformatics* **26**, 139–140 (2010).

108. Love, M. I., Huber, W. & Anders, S. Moderated estimation of fold change and dispersion for RNA-seq data with DESeq2. *Genome Biol* **15**, 1–21 (2014).

109. Escher, C. *et al.* Using iRT, a normalized retention time for more targeted measurement of peptides. *Proteomics* **12**, 1111–1121 (2012).

110. Kong, A. T., Leprevost, F. v., Avtonomov, D. M., Mellacheruvu, D. & Nesvizhskii, A. I. MSFragger: ultrafast and comprehensive peptide identification in mass spectrometry–based proteomics. *Nature Methods 2017 14:5* **14**, 513–520 (2017).

111. Teo, G. C., Polasky, D. A., Yu, F. & Nesvizhskii, A. I. Fast Deisotoping Algorithm and Its Implementation in the MSFragger Search Engine. *J Proteome Res* **20**, 498–505 (2021).

bioRxiv preprint doi: https://doi.org/10.1101/2023.05.07.539748; this version posted May 8, 2023. The copyright holder for this preprint (which was not certified by peer review) is the author/funder, who has granted bioRxiv a license to display the preprint in perpetuity. It is made available under aCC-BY-NC-ND 4.0 International license.

112. Yu, F., Haynes, S. E. & Nesvizhskii, A. I. IonQuant enables accurate and sensitive label-free quantification with FDR-controlled match-between-runs. *Molecular and Cellular Proteomics* **20**, 100077 (2021).

113. da Veiga Leprevost, F. *et al.* Philosopher: a versatile toolkit for shotgun proteomics data analysis. *Nature Methods 2020 17:9* **17**, 869–870 (2020).

114. The Bowhead Whale Genome Resource. http://www.bowhead-whale.org/.

115. Haas, B. J. *et al.* De novo transcript sequence reconstruction from RNA-seq using the Trinity platform for reference generation and analysis. *Nature Protocols 2013 8:8* **8**, 1494–1512 (2013).

116. Grabherr, M. G. *et al.* Full-length transcriptome assembly from RNA-Seq data without a reference genome. *Nature Biotechnology 2011 29:7* **29**, 644–652 (2011).

117. Bateman, A. *et al.* UniProt: the universal protein knowledgebase in 2021. *Nucleic Acids Res* **49**, D480–D489 (2021).

118. Elias, J. E. & Gygi, S. P. Target-decoy search strategy for increased confidence in large-scale protein identifications by mass spectrometry. *Nature Methods 2007 4:3* **4**, 207–214 (2007).

bioRxiv preprint doi: https://doi.org/10.1101/2023.05.07.539748; this version posted May 8, 2023. The copyright holder for this preprint (which was not certified by peer review) is the author/funder, who has granted bioRxiv a license to display the preprint in perpetuity. It is made available under aCC-BY-NC-ND 4.0 International license.

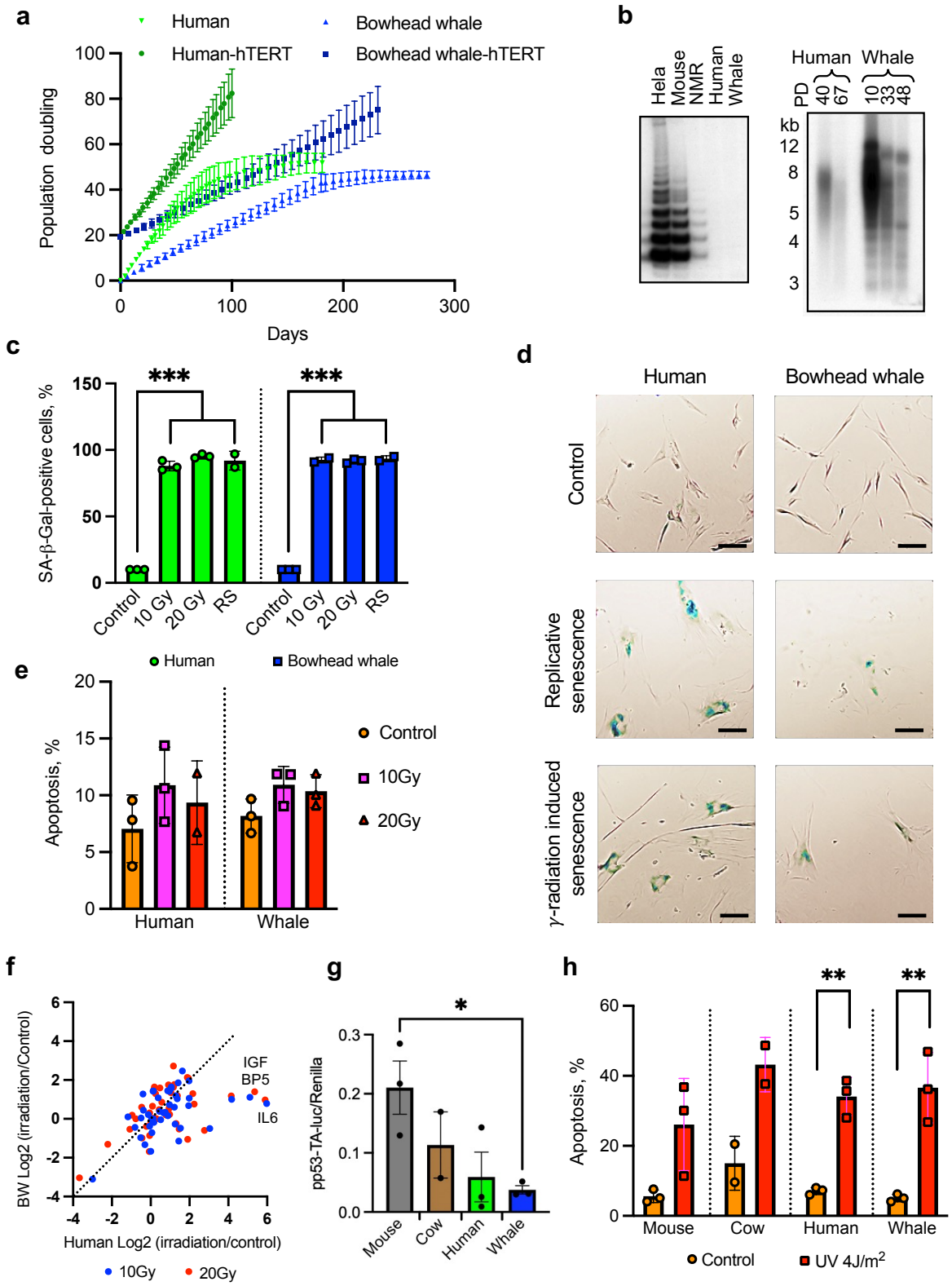

Figure 1. Bowhead whale fibroblasts exhibit senescence with reduced SASP and low p53 activity. a, Growth curves of primary and hTERT-immortalized skin fibroblasts

bioRxiv preprint doi: https://doi.org/10.1101/2023.05.07.539748; this version posted May 8, 2023. The copyright holder for this preprint (which was not certified by peer review) is the author/funder, who has granted bioRxiv a license to display the preprint in perpetuity. It is made available under aCC-BY-NC-ND 4.0 International license.

(n=2 for each cell line). **b**, Telomerase activity and telomere length in skin fibroblasts. **c**, Quantification of β-gal–positive human and bowhead skin fibroblasts in response to γ-irradiation (12 days) and replicative senescence (n=3 for each species). **d**, Representative images of SA-β-gal staining of human and bowhead skin fibroblasts in response to γ-irradiation and replicative senescence. The bar is 100 μm. **e**, Apoptosis of human and bowhead whale fibroblasts in response to γ-irradiation. Three days after γ-irradiation, cells were harvested and subjected to an Annexin V apoptosis assay using flow cytometry (n=3 for each species). **f**, Log fold change of SASP mRNA expression in human and bowhead whale skin fibroblasts 12 days after γ-irradiation. **g**, Relative luciferase expression in mouse, cow, human and bowhead whale fibroblasts transfected with the p53 reporter vector. Data are shown as ratios of firefly/renilla luciferase (to normalize for transfection efficiency) expression 24 h after transfections (n=3 for mouse, human, BW; n=2 for cow). **h**, Apoptosis of mouse, cow, human and bowhead whale fibroblasts in response to UVC. Two days after UVC, cells were harvested and subjected to an Annexin V apoptosis assay using flow cytometry. Error bars represent mean ± SD. * $p<0.05$, ** $p<0.01$, *** $p<0.001$. Two-tailed t-test was used to quantify the significance. Whale, bowhead whale; NMR, naked mole-rat.

bioRxiv preprint doi: https://doi.org/10.1101/2023.05.07.539748; this version posted May 8, 2023. The copyright holder for this preprint (which was not certified by peer review) is the author/funder, who has granted bioRxiv a license to display the preprint in perpetuity. It is made available under aCC-BY-NC-ND 4.0 International license.

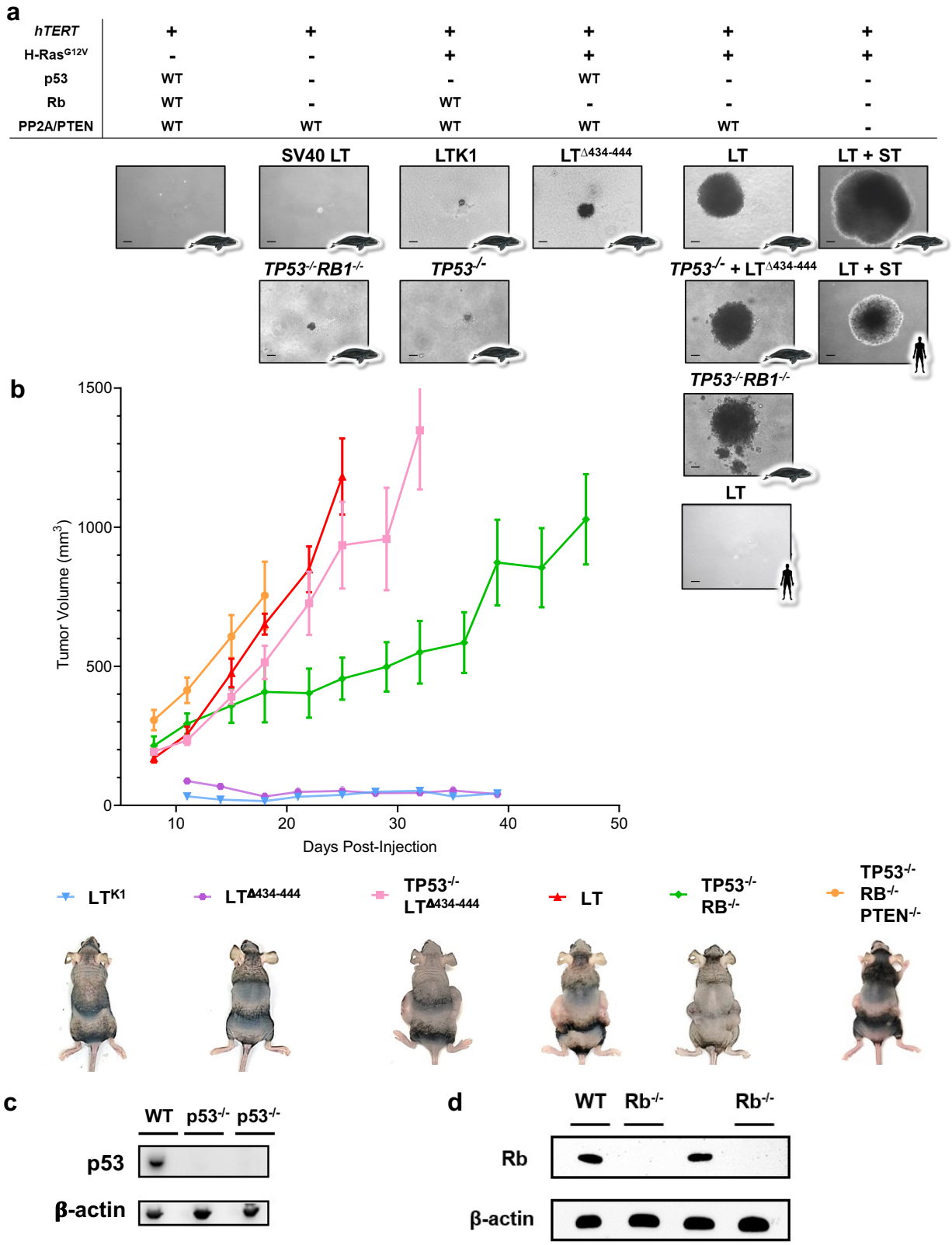

bioRxiv preprint doi: https://doi.org/10.1101/2023.05.07.539748; this version posted May 8, 2023. The copyright holder for this preprint (which was not certified by peer review) is the author/funder, who has granted bioRxiv a license to display the preprint in perpetuity. It is made available under aCC-BY-NC-ND 4.0 International license.

Figure 2. Fewer hits are required for oncogenic transformation of bowhead whale fibroblasts than for human fibroblasts. a, Images of representative fibroblast colonies for tested cell lines after 4 weeks of growth in soft agar. The top panel indicates whether the cell lines in the column below have the indicated protein overexpressed (+), inactivated (-), or expressed in the active endogenous form (WT). Text above individual images indicate for that cell line whether tumor suppressors are inactivated through genetic knockout or SV40 Large T (or LT mutants) or Small T (ST) antigen. Icons in corners of images indicate species. Scale bar is 250 µm. **b**, Volumetric growth curves for the indicated bowhead whale fibroblast cell lines in mouse xenograft assays. All cell lines shown stably express H-Ras^{G12V} and *hTERT* in addition to the genotype indicated in the figure legend. Data points represent averages from 3 immunodeficient nude mice injected bilaterally (6 injections) for each cell line, except for *TP53*$^{-/-}$*RB1*$^{-/-}$ double knockouts, for which 2 independent cell lines were tested, for a total of 6 mice/12 injections. Experiments were terminated based on endpoints for maximum tumor size or duration of experiment as described in Methods. Images in the legend show a representative mouse for the indicated cell line at the final measured time point. Error bars show SEM. **c**, Western blot for p53 protein in clonally isolated fibroblast colonies following CRISPR targeting of *TP53*. Underlined lanes indicate colonies selected for further validation and experiments. **d**, Western blot for Rb protein in fibroblast clones following CRISPR targeting of *RB1* on an p53 knockout background.

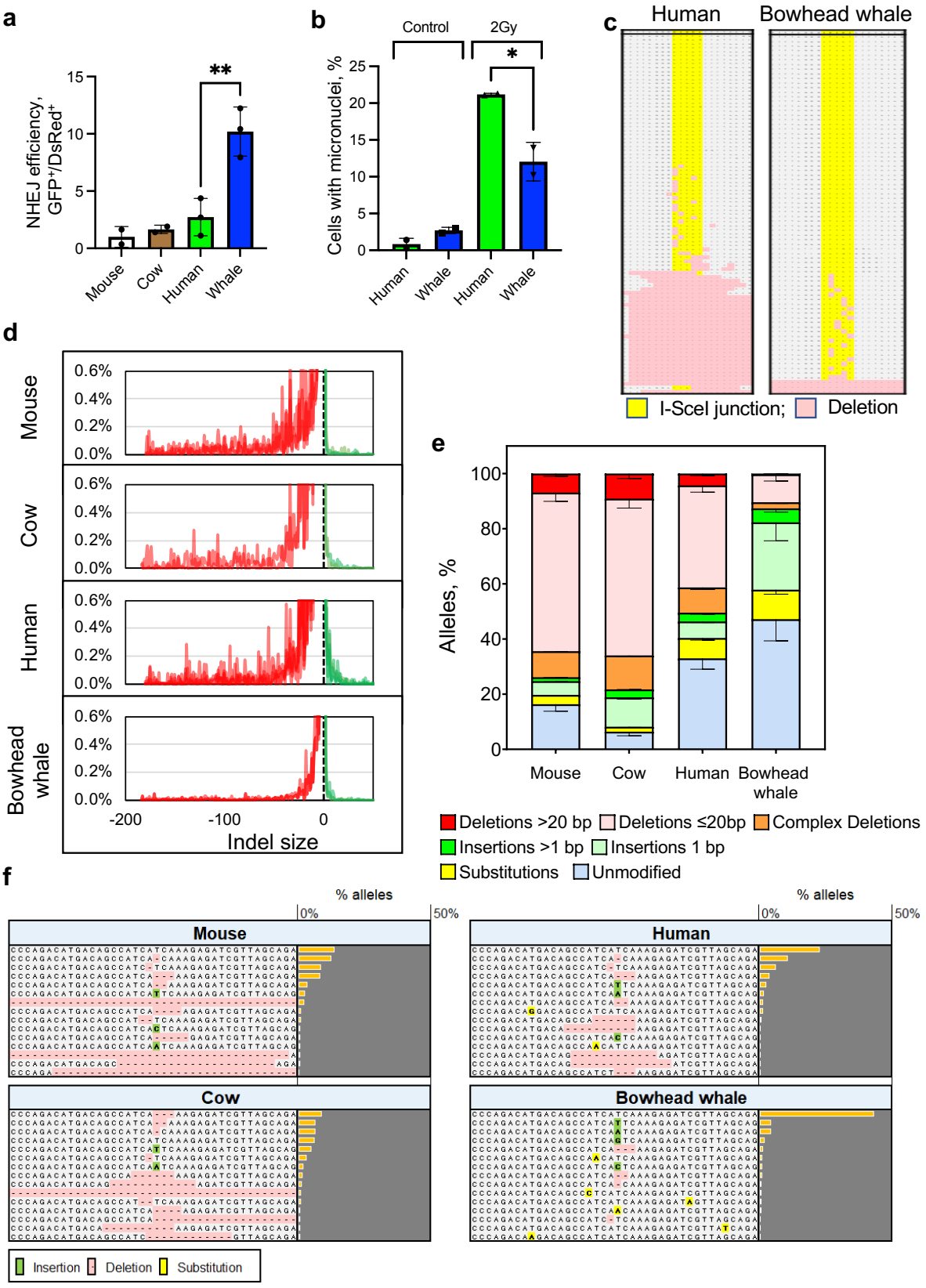
a
NHEJ efficiency, GFP+/DsRed+
15
10
5
0
**
Mouse
Cow
Human
Whale
b
Control
2Gy
Cells with micronuclei, %
25
20
15
10
5
0
*
Human
Whale
Human
Whale
c
Human
Bowhead whale
I-SceI junction;
Deletion
d
Mouse
Cow
Human
Bowhead whale
0.6%
0.4%
0.2%
0.0%
-200
-100
0
Indel size
e
Alleles, %
100
80
60
40
20
0
Mouse
Cow
Human
Bowhead whale
Deletions >20 bp
Deletions ≤20bp
Complex Deletions
Insertions >1 bp
Insertions 1 bp
Substitutions
Unmodified
f
% alleles
0%
50%
Mouse
Human
Cow
Bowhead whale
Insertion
Deletion
Substitution

Figure 3. The bowhead whale repairs DSBs with higher accuracy and efficiency than other mammals. a, NHEJ efficiency was measured using fluorescent reporter construct where GFP gene is interrupted by a "killer" exon flanked by I-SceI sites (Extended Data Figure 3a). DSB induction by I-SceI removes the exon and successful NHEJ event leads to reactivation of the GFP gene. NHEJ reporter construct was integrated into primary, low passage skin fibroblasts. NHEJ repair efficiency was assayed by transfecting cells with I-SceI expression vector and a DsRed plasmid as a transfection control. The repair efficiency was calculated as the ratio of GFP+/DsRed+ cells. Experiments were repeated at least 3 times for each cell line. **b**, % binucleated cells containing micronuclei in human and bowhead whale fibroblasts after 2Gy γ-irradiation. Error bars represent SD (n=2). **c**, Allele plot of Sanger sequencing products resulting from repair of integrated NHEJ reporter cassette after I-SceI cleavage. **d**, Histograms of CRISPR indel size distribution by species. Data for biological replicates are superimposed and partially transparent with lines connecting data points for each sample. Unmodified alleles and alleles with substitutions only are excluded from this analysis. **e**, Distribution of sequenced PTEN allele variants by species after CRISPR DSB induction at a conserved region of the endogenous PTEN gene. Data are averages from multiple primary dermal fibroblast lines isolated from different individual animals for bowhead whale (n=3), human (n=3), cow (n=2), and mouse (n=3). Error bars represent SEM. **f**, Allele plots showing 15 most frequent allele types after CRISPR for one representative cell line per species. Sequences are displayed within a window centered on the cleavage site and extending 20 bp in each direction. Data bars and values indicate proportion of total alleles represented by each row. For the purposes of this display and quantification, all individual alleles with identical sequences in the 40-bp window have been pooled, so rows represent composites of alleles that may differ outside the display window. Error bars represent SD. * $p<0.05$, ** $p<0.01$ (two-tailed t-test). Whale, bowhead whale.

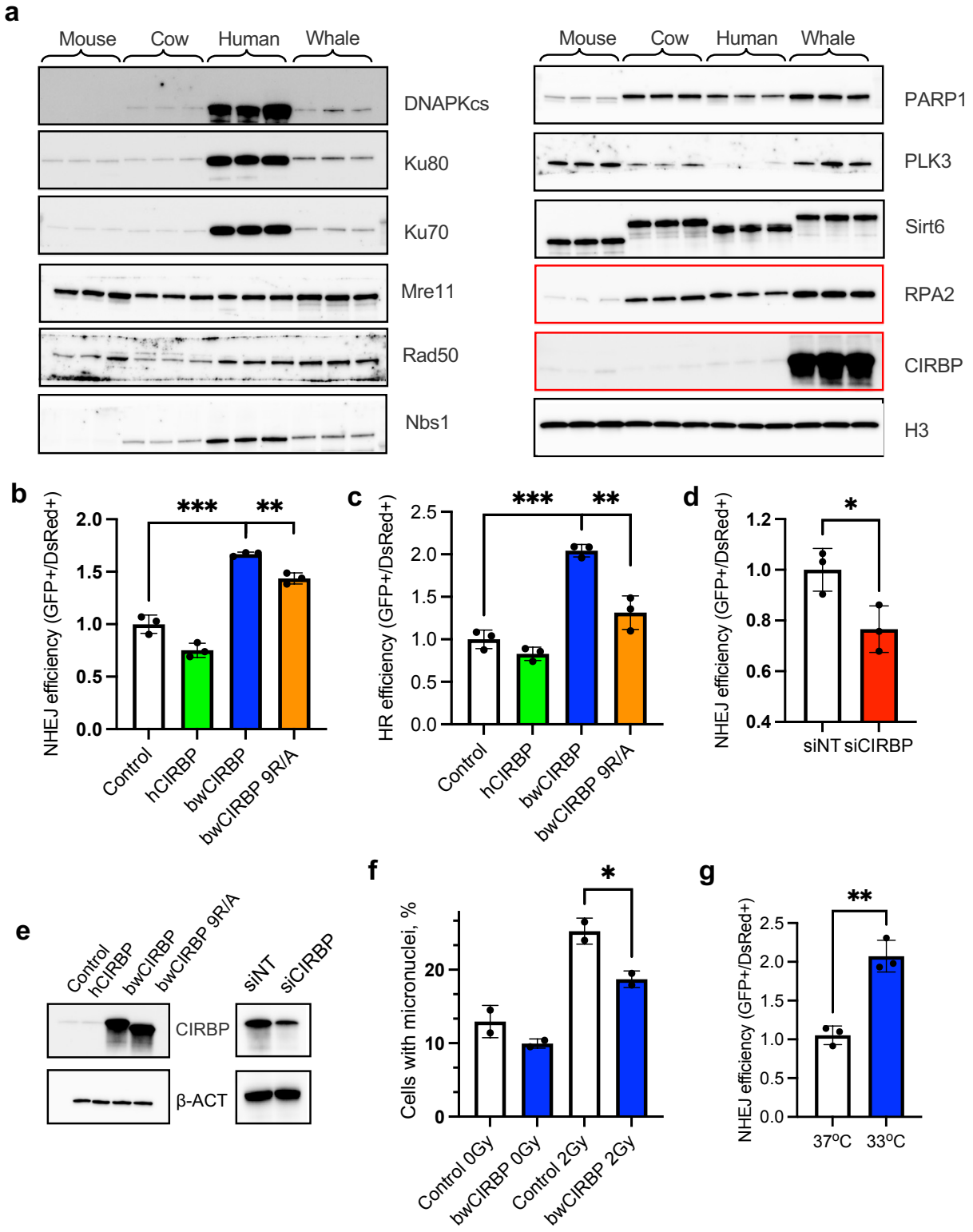

Figure 4. CIRBP is highly expressed in bowhead whale fibroblasts and promotes genomic stability. a, Western blots of DNA repair proteins in primary fibroblasts from different species. **b-c**, bwCIRBP promotes NHEJ and HR in human cells as measured by

flow cytometric GFP-reporter assays (see Methods). In these assays DSBs are induced within inactive NHEJ or HR reporter cassettes by expressing I-SceI endonuclease. Successful NHEJ or HR events lead to reactivation of the fluorescent GFP reporters that are scored by flow cytometry. All experiments in these figures were repeated at least 3 times. **d**, Knockdown of CIRBP in bowhead whale fibroblasts decreases NHEJ efficiency. Cells were transfected with siRNA 3d before I-Sce1 transfection. **e**, Western blot of human fibroblasts overexpressing human CIRBP, whale CIRBP or 9R/A mutated whale CIRBP (left panel); and bowhead whale fibroblasts with knockdown of CIRBP (right panel). **f**, Overexpression of bwCIRBP decreases the percentage of human cells containing micronuclei 3d after 2Gy γ-irradiation (n=2). **g**, Hypothermia promotes NHEJ efficiency in primary human fibroblasts. Cells were pre-incubated at 33°C for 2 days, co-transfected with I-SceI-digested NHEJ reporter and DsRed, and returned to the 33°C incubator. NHEJ efficiency was measured by flow cytometry 3 days following transfection (n=3). Error bars represent mean ± SD. * $p<0.05$, ** $p<0.01$, *** $p<0.001$ (two-tailed t-test).

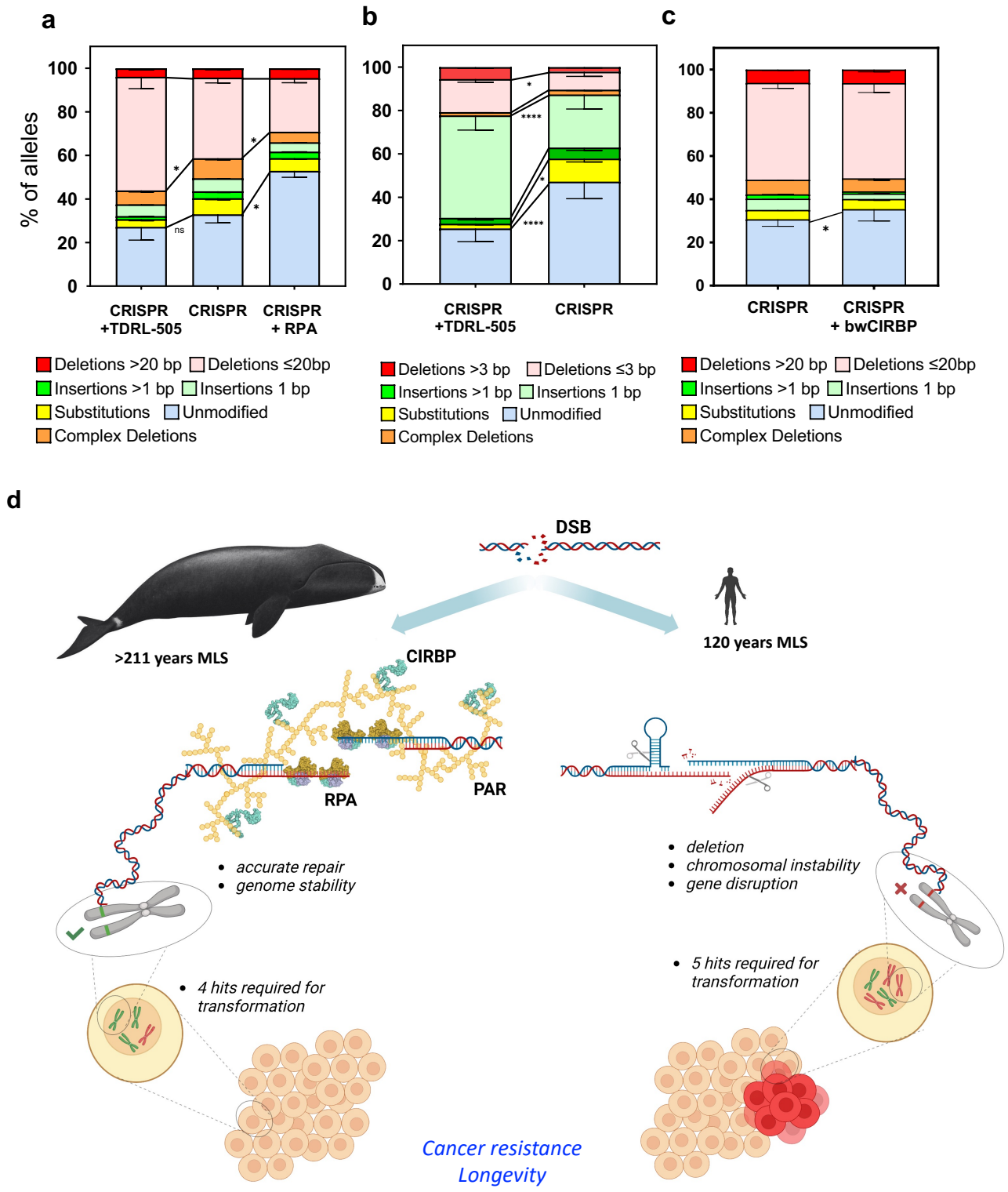

Figure 5. RPA and CIRBP contribute to increased DNA repair fidelity. a, Distribution of sequenced PTEN allele variants in human primary fibroblasts treated with RPA inhibitor TDRL-505 or transfected with human RPA complex after CRISPR DSB induction at a

conserved region of the endogenous PTEN gene. **b**, Distribution of sequenced PTEN allele variants by species in bowhead whale primary fibroblasts treated with TDRL-505 after CRISPR DSB induction in PTEN gene. **c**, Distribution of sequenced PTEN allele variants by species in human fibroblasts with lentiviral overexpression of luciferase or bwCIRBP after CRISPR DSB induction in endogenous PTEN gene. (**a-c**) Data are averages from experiments performed in triplicate. Error bars represent SEM. * $p<0.05$, **** $p<0.0001$. All charts analyzed by two-way ANOVA with Fisher's LSD.

d, Graphical summary. Bowhead whale has evolved very efficient and accurate DSB repair that is mediated by high protein levels of CIRBP, RPA2 and high PARP activity. This enhanced DNA repair may help bowhead whale achieve cancer resistance despite fewer mutational hits required for malignant transformation of whale cells as compared to human cells. The strategy of enhanced repair rather than enhanced elimination of damaged cells through apoptosis or senescence may benefit the extreme longevity of the bowhead whale.

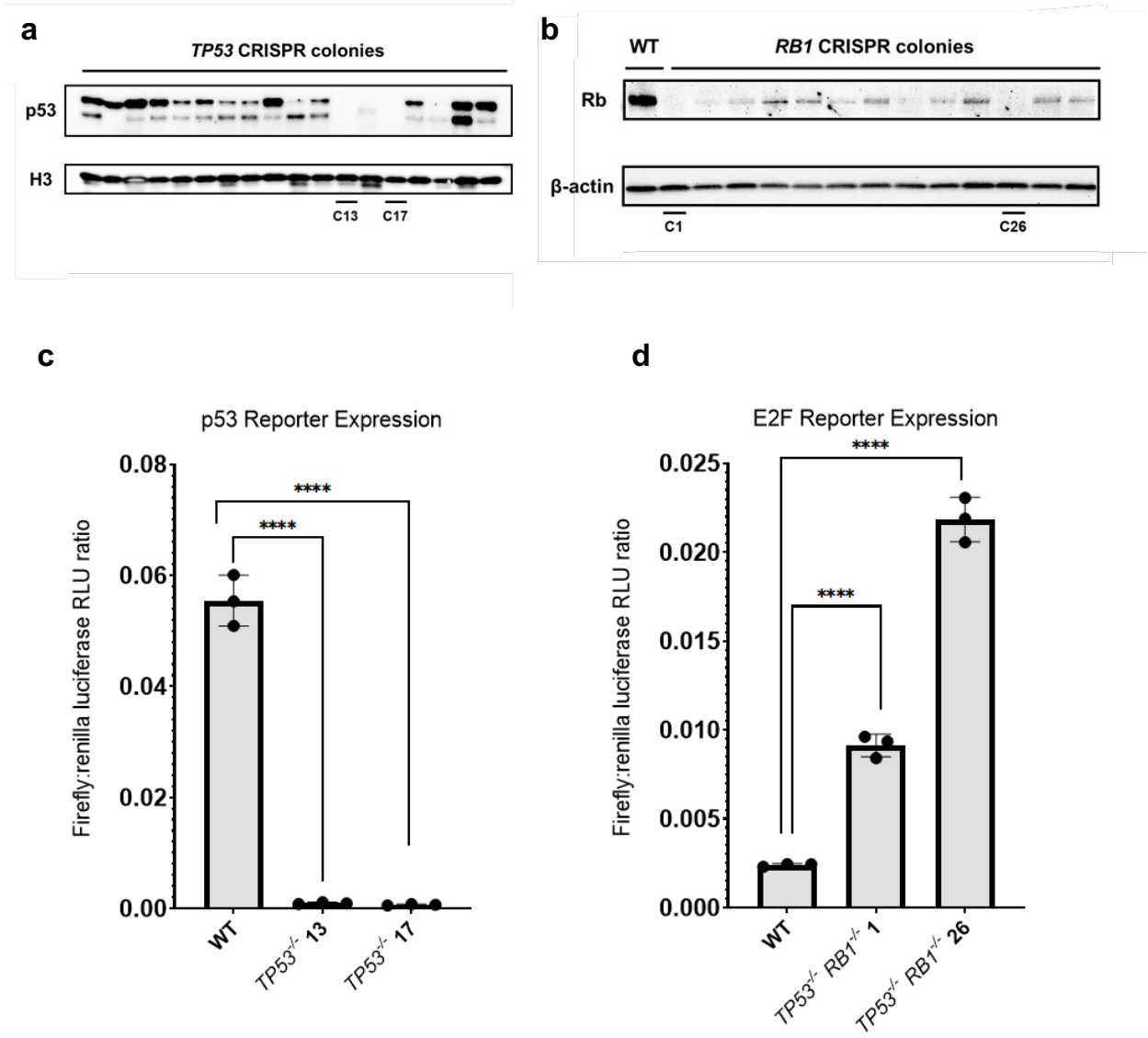

Extended Data Figure 1. Characterization of p53 and Rb knockout cell lines. a, Western blot for p53 protein in fibroblasts clones following CRISPR targeting of *TP53*. Labeled clones were for further validation and experiments. **b**, Western blot for Rb protein in fibroblast clones following CRISPR targeting of *RB1* on p53 knockout background. **c**, Ratio of firefly:renilla luciferase luminescence in fibroblasts transfected with firefly luciferase reporter of p53 transcriptional activity and renilla luciferase control. Cells were treated with etoposide to induce p53 activity. **d**, Ratio of firefly:renilla luciferase luminescence in fibroblasts transfected with firefly luciferase reporter of E2F transcriptional activity and renilla luciferase control. Transfected cells were serum starved for 24h and returned to complete medium for 24h before luminescence measurement. Higher E2F activity results from reduced Rb activity. Error bars represent SD. ****$p<0.001$ (two-tailed t test), n=3.

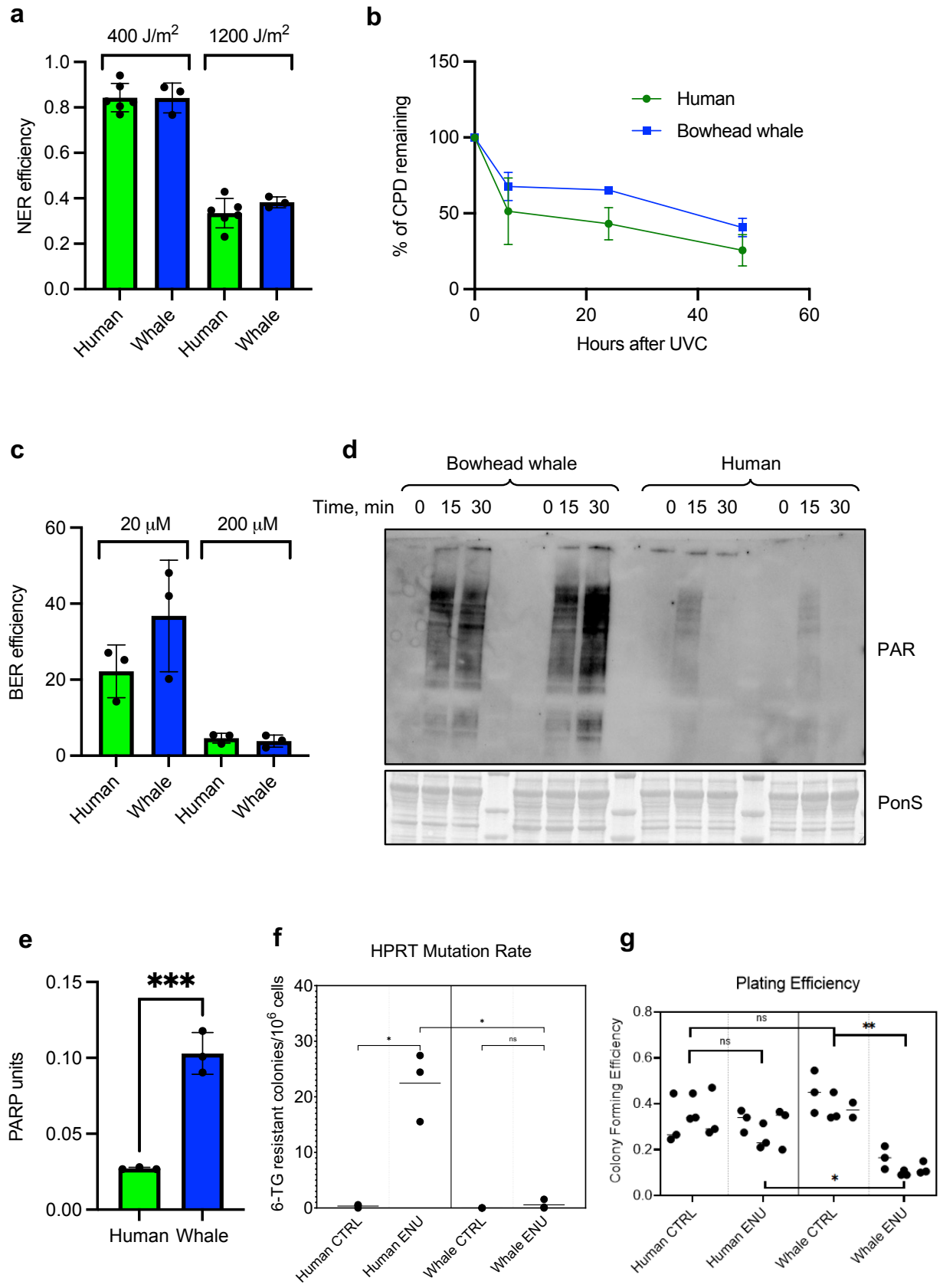
a
400 J/m2
1200 J/m2
NER efficiency
1.0
0.8
0.6
0.4
0.2
0.0
Human
Whale
Human
Whale
b
% of CPD remaining
150
100
50
0
Human
Bowhead whale
0
20
40
60
Hours after UVC
c
20 μM
200 μM
BER efficiency
60
40
20
0
Human
Whale
Human
Whale
d
Bowhead whale
Human
Time, min
0 15 30
0 15 30
0 15 30
0 15 30
PAR
PonS
e
***
PARP units
0.15
0.10
0.05
0.00
Human
Whale
f
HPRT Mutation Rate
6-TG resistant colonies/10^6 cells
40
30
20
10
0
*
*
ns
Human CTRL
Human ENU
Whale CTRL
Whale ENU
g
Plating Efficiency
Colony Forming Efficiency
0.8
0.6
0.4
0.2
0.0
ns
ns
**
*
Human CTRL
Human ENU
Whale CTRL
Whale ENU

Extended Data Figure 2. Analysis of NER and BER in bowhead whale cells. a, NER efficiency was measured by host cell reactivation assay where a plasmid containing luciferase reporter is UV-irradiated *in vitro* to induce DNA damage, transfected into cells, and reactivation of the reporter is measured (n=3 for each cell line). **b**, Kinetics of cyclobutane pyrimidine dimer repair after 30 J/m^2 UVC. Confluent human and whale skin fibroblasts were subjected to UVC, harvested at different time-points, genomic DNA was isolated and analyzed for cyclobutene dimers as described in Methods (n=2 for each cell line). **c**, BER efficiency was measured by host cell reactivation where luciferase reporter plasmid is treated with methylene blue and light to induce oxidative DNA damage, transfected into cells, and luciferase activity measured as described in Methods. **d**, Bowhead whale cells show greater poly-ADP-ribosylation in response to hydrogen peroxide treatment. **e**, Nuclear extracts of bowhead whale fibroblasts exhibit higher basal PARP activity (n=3). **f**, HPRT mutagenesis assay, adjusted by plating efficiency measured for each cell line. **g**, Colony forming efficiency for HPRT mutagenesis assay. Error bars represent mean ± SD. * $p<0.05$, ** $p<0.01$, *** $p<0.001$, ns=not significant (two-tailed t-test).

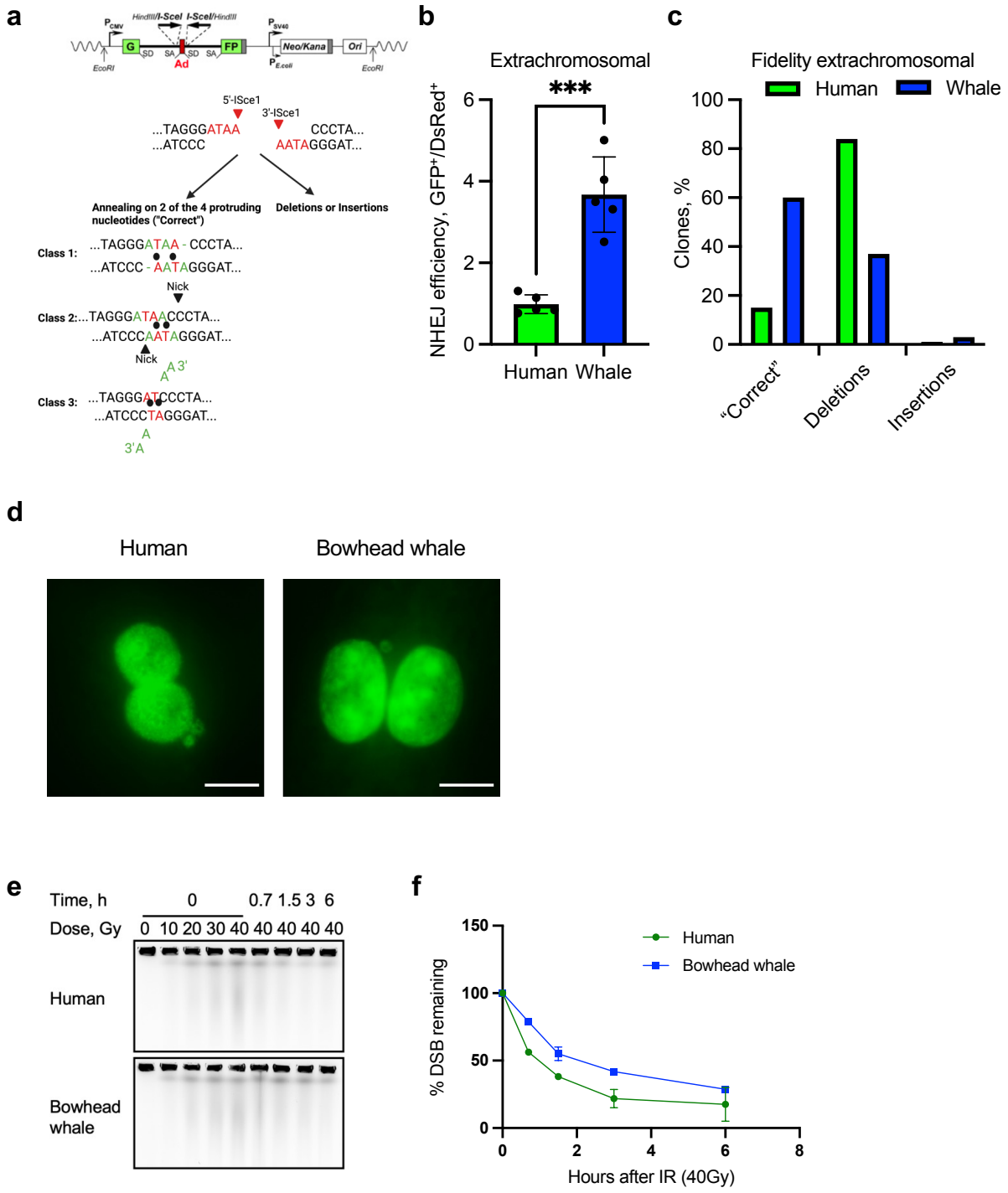

Extended Data Figure 3. Analysis of DSB repair in bowhead whale cells. a, Possible repair outcomes after induction of DSBs with incompatible ends by I-SceI in NHEJ reporter construct. **b**, NHEJ efficiency in extrachromosomal assay. NHEJ reporter construct was pre-digested with I-SceI, purified and co-transfected with DsRed into human and bowhead skin fibroblasts. Three days after transfection cells were harvested and subjected to flow cytometry to calculate NHEJ efficiency (n=3). **c**, NHEJ fidelity in

extrachromosomal assay. Immediately after FACS/flow cytometry, genomic DNA was isolated, subjected to PCR, cloned and analyzed by Sanger sequencing. At least 100 clones were analyzed for each species. **d**, Representative images of human and bowhead whale binucleated cells containing micronuclei after 2 Gy of γ-irradiation. Scale bar is 20 μm. **e**, Pulse-field gel stained with ethidium bromide, showing chromosomal DNA fragmentation in human and bowhead confluent skin fibroblasts immediately after different doses of γ-irradiation 0.7, 1.5, 3 and 6h after 40 Gy of γ-irradiation. **f**, Kinetics of DSB repair measured by PFGE in confluent human and bowhead fibroblasts after 40 Gy of γ-irradiation. n=2 for each species. Error bars represent mean ± SD. *** $p<0.001$ (two-tailed t-test).

a

```
            1                                                                                   82
Consensus   TGGCTGCTGAGGAGAAGCAGGCCCAGTCGCTGCAACCATCCAGCAGCCGCCGCAGCAGCCATTACCCGGCTGCGGTCCAGAG
Whale       TGGCTGCTGAGGAGAAGCAGGCCCAGTCGCTGCAACCATCCAGCAGCCGCCGCAGCAGCCATTACCCGGCTGCTGTCCAGAT
Cow         TGGCTGCTGAGGAGAAGCAGGCCCAGTCGCTGCAACCATCCAGCAGCCGCCGCAGCAGCCATTACCCGGCTGCGGTCCAGAG
Human       TGGCTGCTGAGGAGAAGCAGGCCCAGTCGCTGCAACCATCCAGCAGCCGCCGCAGCAGCCATTACCCGGCTGCGGTCCAGAG
Mouse       TGGCTGCTGAGGAGAAGCAGGCCCAGTCTCTGCAACCATCCAGCAGCCGCCGCAGCAGCCATTACCCGGCTGCGGTCCAGGG
PTEN Exon 1 ----------------------------------------------------------------------------------
Guide Site  ----------------------------------------------------------------------------------

            83                                                                                 164
Consensus   CCAAGCGGCAGCAGAGCGAGGGGCATCAGCCACCGCCAAGTCCAGAGCCATTTCCATCCTGCAGAAGAAGCCCCGCCACCAG
Whale       CCAAGCGGCAGCAGAGCGAGGGGCATCAGCCACCGCCAAGTCCAGAGCCATTTCCATCCTGCAGAAGAAGCCCCGCCACCAG
Cow         CCAAGCGGCAGCAGAGCGAGGGGCATCAGCCACCGCCAAGTCCAGAGCCATTTCCATCCTGCAGAAGAAGCCCCGCCACCAG
Human       CCAAGCGGCGGCAGAGCGAGGGGCATCAGCTACCGCCAAGTCCAGAGCCATTTCCATCCTGCAGAAGAAGCCCCGCCACCAG
Mouse       CCAAGCGGCAGCAGAGCGAGGGGCATCAGCGACCGCCAAGTCCAGAGCCATTTCCATCCTGCAGAAGAAGCCTCGCCACCAG
PTEN Exon 1 ----------------------------------------------------------------------------------
Guide Site  ----------------------------------------------------------------------------------

            165                                                                                246
Consensus   CAGCTTCTGCCATCTCTCTCCTCCTTTTTCTTCAGCCACAGGCTCCCAGACATGACAGCCATCATCAAAGAGATCGTTAGCA
Whale       CAGCTTCTGCCATCTCTCTCCTCCTTTTTCTTCAGCCACAGGCTCCCAGACATGACAGCCATCATCAAAGAGATCGTTAGCA
Cow         CAGCTTCTGCCATCTCTCTCCTCCTTTTTCTTCAGCCACAGGCTCCCAGACATGACAGCCATCATCAAAGAGATCGTTAGCA
Human       CAGCTTCTGCCATCTCTCTCCTCCTTTTTCTTCAGCCACAGGCTCCCAGACATGACAGCCATCATCAAAGAGATCGTTAGCA
Mouse       CAGCTTCTGCCATCTCTCTCCTCCTTTTTCTTCAGCCACAGGCTCCCAGACATGACAGCCATCATCAAAGAGATCGTTAGCA
PTEN Exon 1 ---------------------------------------------------ATGACAGCCATCATCAAAGAGATCGTTAGCA
Guide Site  ------------------------------------------------------------TCATCAAAGAGATCGTTAGC-

            247                                                                                328
Consensus   GAAACAAAAGGAGATATCAAGAGGATGGATTCGACTTAGACTTGACCTGTATCCATTTCTGCGGCTGCCGCTCCTCTTTGCC
Whale       GAAACAAAAGGAGATATCAAGAGGATGGATTCGACTTAGACTTGACCTGTATCCATTTCTGTGGCTGCCGCTCCTCTTTGCC
Cow         GAAACAAAAGGAGATATCAAGAGGATGGATTCGACTTAGACTTGACCTGTATCCATTTCTGTGGCTGCTGTTCCTCTTTGCC
Human       GAAACAAAAGGAGATATCAAGAGGATGGATTCGACTTAGACTTGACCTGTATCCATTTCTGCGGCTGC---TCCTCTTTACC
Mouse       GAAACAAAAGGAGATATCAAGAGGATGGATTCGACTTAGACTTGACCTGTATCCATTTCTGCGGCTGT---TCCTCTTTGCT
PTEN Exon 1 GAAACAAAAGGAGATATCAAGAGGATGGATTCGACTTAGACTTGACCT-----------------------------------
Guide Site  ----------------------------------------------------------------------------------

            329                                       369
Consensus   TTTCTGTCACTCTCTCTTATAACGTGGGAGTAGACGGATGC
Whale       TTTCTGTCACTCTCTCTTATAACGTGGGAGTAGACGGATGC
Cow         TTTCTGTCACTCTCTCTGATAACGTGGGATTAGACGGATGC
Human       TTTCTGTCACT--CTCTTAGAACGTGGGAGTAGACGGATGC
Mouse       TTTCTGTCA----CTCTGATAACGTGGGAGTAGACGGATGC
PTEN Exon 1 ------------------------------------------
Guide Site  ------------------------------------------
```

b

Mouse

```
CCCAGACATGACAGCCATCATCAAAGAGATCGTTAGCAGA-Reference
                sgRNA

CCCAGACATGACAGCCATCATCAAAGAGATCGTTAGCAGA-86.05% (33259 reads)
CCCAGACATGACGGCCATCATCAAAGAGATCGTTAGCAGA-0.50% (195 reads)
CCCAGACATGACAGCCATCACCAAAGAGATCGTTAGCAGA-0.48% (185 reads)
CCCAGACATGGCAGCCATCATCAAAGAGATCGTTAGCAGA-0.46% (178 reads)
CCCAGACATGACAGCCATCATCAAAGGGATCGTTAGCAGA-0.46% (177 reads)
CCCAGACATGACAGCCATCATCAAGGGATCGTTAGCAGA-0.46% (176 reads)
CCCAGACACGACAGCCATCATCAAAGAGATCGTTAGCAGA-0.44% (170 reads)
CCCAGACATGACAGCCATCATCAGAGAGATCGTTAGCAGA-0.43% (168 reads)
CCCAGACATGACAGCCATCATCAAAGAGGTCGTTAGCAGA-0.42% (162 reads)
CCCAGACATGACAGCCATCATCAAAGAGATCGTTAGCAGG-0.40% (156 reads)
CCCAGACGTGACAGCCATCATCAAAGAGATCGTTAGCAGA-0.39% (152 reads)
CCCAGACATGACAGCCATCATCGAAGAGATCGTTAGCAGA-0.39% (151 reads)
CCCAGACATGACAGCCATCATCAAAGAGATCGCTAGCAGA-0.36% (139 reads)
CCCGGACATGACAGCCATCATCAAAGAGATCGTTAGCAGA-0.35% (136 reads)
CCCAGGCATGACAGCCATCATCAAAGAGATCGTTAGCAGA-0.35% (136 reads)
CCCAGACATGACAGCCATCGTCAAAGAGATCGTTAGCAGA-0.32% (124 reads)
CCCAGACATGACAGCCACCATCAAAGAGATCGTTAGCAGA-0.32% (122 reads)
CCCAGACATGACAGCCATCATCAAAGAGATCGTTAGCGGA-0.31% (121 reads)
CCCAGACATGACAGCCATCATCAAAGAGACCGTTAGCAGA-0.30% (116 reads)
CCCAGACATGACAGCCGTCATCAAAGAGATCGTTAGCAGA-0.28% (107 reads)
CCCAGACATGACAGCCATCATCAAAGAGATCGTCAGCAGA-0.27% (104 reads)
CCCAGACATGACAGCCATCATCAAAGAGATCGTTGGCAGA-0.21% (82 reads)
```

bold Substitutions
Insertions
Deletions
------ Predicted cleavage position

Cow

```
CCCAGACATGACAGCCATCATCAAAGAGATCGTTAGCAGA-Reference
                sgRNA

CCCAGACATGACAGCCATCATCAAAGAGATCGTTAGCAGA-88.56% (112527 reads)
CCCAGACATGGCAGCCATCATCAAAGAGATCGTTAGCAGA-0.33% (423 reads)
CCCAGACATGACGGCCATCATCAAAGAGATCGTTAGCAGA-0.33% (421 reads)
CCCAGACATGACAGCCATCATCAGAGAGATCGTTAGCAGA-0.32% (412 reads)
CCCAGACATGACAGCCATCATCAAGGAGATCGTTAGCAGA-0.32% (412 reads)
CCCAGACAGTGACAGCCATCATCAAAGAGATCGTTAGCAGA-0.32% (407 reads)
CCCAGACACGACAGCCATCATCAAAGAGATCGTTAGCAGA-0.30% (377 reads)
CCCAGACATGACAGCCATCATCAAAGAGATCGTTAGCAGG-0.29% (373 reads)
CCCAGACATGACAGCCATCATCCAAAGAGATCGTTAGCAGA-0.29% (373 reads)
CCCAGACATGACAGCCATCATCGAAGAGATCGTTAGCAGA-0.28% (359 reads)
CCCAGACATGACAGCCATCATCAAAGAGGTCGTTAGCAGA-0.28% (355 reads)
CCCAGACATGACAGCCATCATCAAAGAGATCGTTAGCGGA-0.27% (347 reads)
CCCAGACATGACAGCCATCATCAAAGGGATCGTTAGCAGA-0.27% (344 reads)
CCCAGACATGACAGCCACCATCAAAGAGATCGTTAGCAGA-0.26% (328 reads)
CCCAGACATGACAGCCATCGTCAAAGAGATCGTTAGCAGA-0.25% (320 reads)
CCCAGGCATGACAGCCATCATCAAAGAGATCGTTAGCAGA-0.25% (319 reads)
CCCAGACATGACAGCCATCATCAAAGAGATCGTCAGCAGA-0.24% (308 reads)
CCCAGACATGACAGCCATCATCAAAGAGATCGCTAGCAGA-0.24% (306 reads)
CCCAGACATGACAGCCATCATCAAAGAGACCGTTAGCAGA-0.23% (290 reads)
CCCAGACATGACAGCCGTCATCAAAGAGATCGTTAGCAGA-0.22% (284 reads)
CCCGGACATGACAGCCATCATCAAAGAGATCGTTAGCAGA-0.22% (277 reads)
```

bold Substitutions
Insertions
Deletions
------ Predicted cleavage position

Human

```
CCCAGACATGACAGCCATCATCAAAGAGATCGTTAGCAGA-Reference
                sgRNA

CCCAGACATGACAGCCATCATCAAAGAGATCGTTAGCAGA-88.34% (56945 reads)
CCCAGACATGACGGCCATCATCAAAGAGATCGTTAGCAGA-0.37% (241 reads)
CCCAGACATGACAGCCATCACCAAAGAGATCGTTAGCAGA-0.37% (239 reads)
CCCAGACACGACAGCCATCATCAAAGAGATCGTTAGCAGA-0.37% (238 reads)
CCCAGACATGGCAGCCATCATCAAAGAGATCGTTAGCAGA-0.36% (233 reads)
CCCAGACATGACAGCCATCATCAAAGGGATCGTTAGCAGA-0.35% (227 reads)
CCCAGACATGACAGCCATCATCAAGGAGATCGTTAGCAGA-0.35% (227 reads)
CCCAGACATGACAGCCATCATCAAAGGGATCGTTAGCAGA-0.34% (221 reads)
CCCAGACATGACAGCCATCATCAAAGAGATCGTTAGCGGA-0.34% (219 reads)
CCCAGACATGACAGCCATCATCAGAGAGATCGTTAGCAGA-0.34% (219 reads)
CCCAGACGTGACAGCCATCATCAAAGAGATCGTTAGCAGA-0.34% (217 reads)
CCCAGGCATGACAGCCATCATCAAAGAGATCGTTAGCAGA-0.32% (205 reads)
CCCAGACATGACAGCCATCATCAAAGAGATCGTTAGCAGG-0.31% (197 reads)
CCCAGACATGACAGCCATCATCGAAGAGATCGTTAGCAGA-0.29% (190 reads)
CCCAGACATGACAGCCATCATCAAAGAGATCGCTAGCAGA-0.27% (177 reads)
CCCAGACATGACAGCCATCATCAAAGAGATCGTCAGCAGA-0.27% (172 reads)
CCCGGACATGACAGCCATCATCAAAGAGATCGTTAGCAGA-0.26% (170 reads)
CCCAGACATGACAGCCACCATCAAAGAGATCGTTAGCAGA-0.26% (165 reads)
CCCAGACATGACAGCCATCATCAAAGAGATCGTTGGCAGA-0.22% (145 reads)
CCCAGACATGACAGCCATCATCAAAGAGACCGTTAGCAGA-0.20% (131 reads)
```

bold Substitutions
Insertions
Deletions
------ Predicted cleavage position

Bowhead whale

```
CCCAGACATGACAGCCATCATCAAAGAGATCGTTAGCAGA-Reference
                sgRNA

CCCAGACATGACAGCCATCATCAAAGAGATCGTTAGCAGA-86.82% (77225 reads)
CCCAGACATGACAGCCATCACCAAAGAGATCGTTAGCAGA-0.41% (367 reads)
CCCAGACATGGCAGCCATCATCAAAGAGATCGTTAGCAGA-0.41% (365 reads)
CCCAGACATGACGGCCATCATCAAAGAGATCGTTAGCAGA-0.39% (347 reads)
CCCAGACATGACAGCCATCATCAAAGGGATCGTTAGCAGA-0.37% (331 reads)
CCCAGACATGACAGCCATCATCAAGGAGATCGTTAGCAGA-0.37% (330 reads)
CCCAGACATGACAGCCATCATCAAAGAGGTCGTTAGCAGA-0.36% (318 reads)
CCCGGACATGACAGCCATCATCAAAGAGATCGTTAGCAGA-0.35% (313 reads)
CCCAGACATGACAGCCATCATCGAAGAGATCGTTAGCAGA-0.35% (312 reads)
CCCAGACATGACAGCCATCATCAAAGAGATCGTTAGCGGA-0.35% (312 reads)
CCCAGACATGACAGCCATCATCAAAGAGATCGTTAGCAGG-0.35% (310 reads)
CCCAGACGTGACAGCCATCATCAAAGAGATCGTTAGCAGA-0.35% (308 reads)
CCCAGACATGACAGCCATCATCAGAGAGATCGTTAGCAGA-0.34% (302 reads)
CCCAGACATGACAGCCACCATCAAAGAGATCGTTAGCAGA-0.34% (299 reads)
CCCAGACACGACAGCCATCATCAAAGAGATCGTTAGCAGA-0.33% (290 reads)
CCCAGGCATGACAGCCATCATCAAAGAGATCGTTAGCAGA-0.32% (289 reads)
CCCAGACATGACAGCCATCGTCAAAGAGATCGTTAGCAGA-0.29% (260 reads)
CCCAGACATGACAGCCGTCATCAAAGAGATCGTTAGCAGA-0.29% (254 reads)
CCCAGACATGACAGCCATCATCAAAGAGACCGTTAGCAGA-0.28% (248 reads)
CCCAGACATGACAGCCATCATCAAAGAGATCGCTAGCAGA-0.28% (248 reads)
CCCAGACATGACAGCCATCATCAAAGAGATCGTCAGCAGA-0.28% (248 reads)
CCCAGACATGACAGCCATCATCAAAGAGATCGTTGGCAGA-0.26% (229 reads)
```

bold Substitutions
Insertions
Deletions
------ Predicted cleavage position

Extended Data Figure 4. *PTEN* sequences used for CRISPR NHEJ assays. a, Alignment of NGS amplicon sequences for each species used to measure NHEJ repair fidelity, showing *PTEN* Exon 1 and guide RNA target site. Amplicon/primer pair was designed based on size appropriate for paired-end sequencing, conservation of internal sequence and primer binding sites, and optimal positioning to detect large deletions. Mismatches to consensus sequence are highlighted in red. Alignments are shown in Benchling with Clustal Omega. **b**, Allele plots from untreated (wild-type) control samples for each species. Plots are outputs from CRISPResso2.

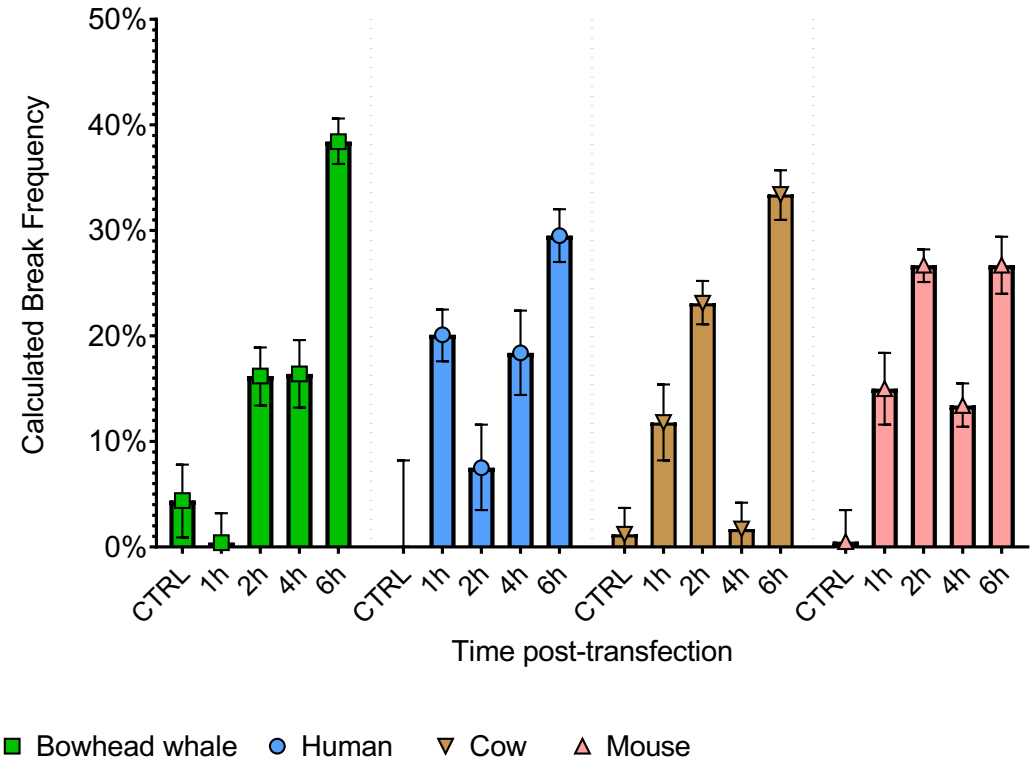

Extended Data Figure 5. Analysis of CRISPR cutting efficiency in different species. Time course of CRISPR cleavage measured by digital droplet PCR (ddPCR). PTEN copy number at varying time points after CRISPR RNP transfection was measured with ddPCR using primers flanking the predicted cleavage site and normalized within each sample to a single-copy genomic ultra-conserved element as described in Methods. Error bars show confidence intervals of Poisson distribution calculated in QuantaSoft. Data are averages from experiments performed in triplicate.

a

	Mouse				Cow			Human				Bowhead whale			
	WTMSF9	WTMSF10	BL6MSF2	Avg.	BT1SF	BT2SF	Avg.	NHDF	HDF637	YAHSF	Avg.	18B9SF	14B10SF	14B11SF	Avg.
1%	-142.0	-140.0	-134.0	**-138.7**	-154.0	-121.0	**-137.5**	-104.0	-126.0	-133.0	**-121.0**	-38.0	-30.0	-68.0	**-45.3**
2%	-110.0	-113.0	-105.0	**-109.3**	-134.0	-82.0	**-108.0**	-63.0	-88.0	-102.0	**-84.3**	-15.0	-14.0	-24.0	**-17.7**
3%	-84.0	-92.0	-80.0	**-85.3**	-112.0	-43.0	**-77.5**	-41.0	-60.0	-71.0	**-57.3**	-10.0	-10.0	-16.0	**-12.0**
4%	-60.0	-80.0	-55.0	**-65.0**	-93.0	-34.0	**-63.5**	-34.0	-37.0	-46.0	**-39.0**	-7.0	-8.0	-11.0	**-8.7**
5%	-44.0	-57.0	-43.0	**-48.0**	-76.0	-31.0	**-53.5**	-29.0	-30.0	-35.0	**-31.3**	-6.0	-6.0	-8.0	**-6.7**
6%	-34.0	-44.0	-34.0	**-37.3**	-54.0	-26.0	**-40.0**	-25.0	-25.0	-30.0	**-26.7**	-4.0	-5.0	-7.0	**-5.3**
7%	-26.0	-38.0	-29.0	**-31.0**	-42.0	-25.0	**-33.5**	-22.0	-23.0	-25.0	**-23.3**	-3.0	-4.0	-6.0	**-4.3**
8%	-21.0	-34.0	-22.0	**-25.7**	-36.0	-22.0	**-29.0**	-21.0	-21.0	-23.0	**-21.7**	-3.0	-3.0	-4.0	**-3.3**
9%	-16.0	-29.0	-18.0	**-21.0**	-31.0	-21.0	**-26.0**	-18.0	-18.0	-22.0	**-19.3**	-3.0	-3.0	-3.0	**-3.0**
10%	-12.0	-25.0	-14.0	**-17.0**	-26.0	-19.0	**-22.5**	-16.0	-16.0	-21.0	**-17.7**	-3.0	-3.0	-3.0	**-3.0**
15%	-4.0	-14.0	-5.0	**-7.7**	-18.0	-12.0	**-15.0**	-10.0	-10.0	-13.0	**-11.0**	-2.0	-3.0	-3.0	**-2.7**
20%	-3.0	-6.0	-3.0	**-4.0**	-12.0	-9.0	**-10.5**	-6.0	-6.0	-10.0	**-7.3**	-1.0	-2.0	-2.0	**-1.7**
25%	-3.0	-4.0	-3.0	**-3.3**	-10.0	-5.0	**-7.5**	-3.0	-3.0	-6.0	**-4.0**	1.0	-1.0	-1.0	**-0.3**
30%	-3.0	-3.0	-3.0	**-3.0**	-7.0	-3.0	**-5.0**	-3.0	-3.0	-4.0	**-3.3**	1.0	-1.0	1.0	**0.3**
35%	-2.0	-3.0	-3.0	**-2.7**	-5.0	-3.0	**-4.0**	-2.0	-2.0	-3.0	**-2.3**	1.0	-1.0	1.0	**0.3**
40%	-2.0	-3.0	-2.0	**-2.3**	-3.0	-3.0	**-3.0**	-1.0	-1.0	-3.0	**-1.7**	1.0	-1.0	1.0	**0.3**
50%	-1.0	-2.0	-1.0	**-1.3**	-3.0	-2.0	**-2.5**	-1.0	-1.0	-3.0	**-1.7**	1.0	1.0	1.0	**1.0**
60%	-1.0	-1.0	-1.0	**-1.0**	-2.0	-1.0	**-1.5**	-1.0	-1.0	-1.0	**-1.0**	1.0	1.0	1.0	**1.0**
70%	-1.0	-1.0	-1.0	**-1.0**	-1.0	-1.0	**-1.0**	-1.0	-1.0	-1.0	**-1.0**	1.0	1.0	1.0	**1.0**
85%	-1.0	-1.0	-1.0	**-1.0**	-1.0	1.0	**0.0**	1.0	-1.0	1.0	**0.3**	1.0	1.0	1.0	**1.0**
90%	-1.0	-1.0	-1.0	**-1.0**	1.0	1.0	**1.0**	1.0	1.0	1.0	**1.0**	1.0	1.0	1.0	**1.0**
95%	1.0	1.0	1.0	**1.0**	1.0	1.0	**1.0**	1.0	1.0	1.0	**1.0**	1.0	1.0	1.0	**1.0**

b

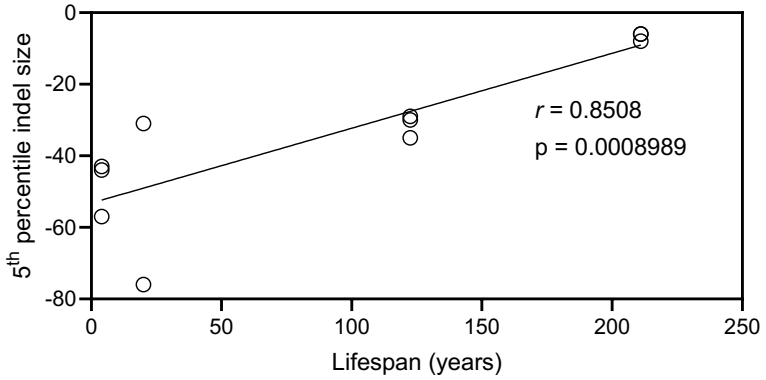

Extended Data Figure 6. CRISPR indel size percentiles. a, Indel size at the specified percentile rank (left column) by cell line and species, based on frequency of each indel size in sequencing data, ranked from most negative (largest deletions) to most positive (largest insertions), with unmodified or substitution-only alleles excluded. **b**, Pearson correlation between 5th percentile indel size and species lifespan (r=0.8508, 95% CI = 0.5125 to 0.9605, p=0.0009, n=11).

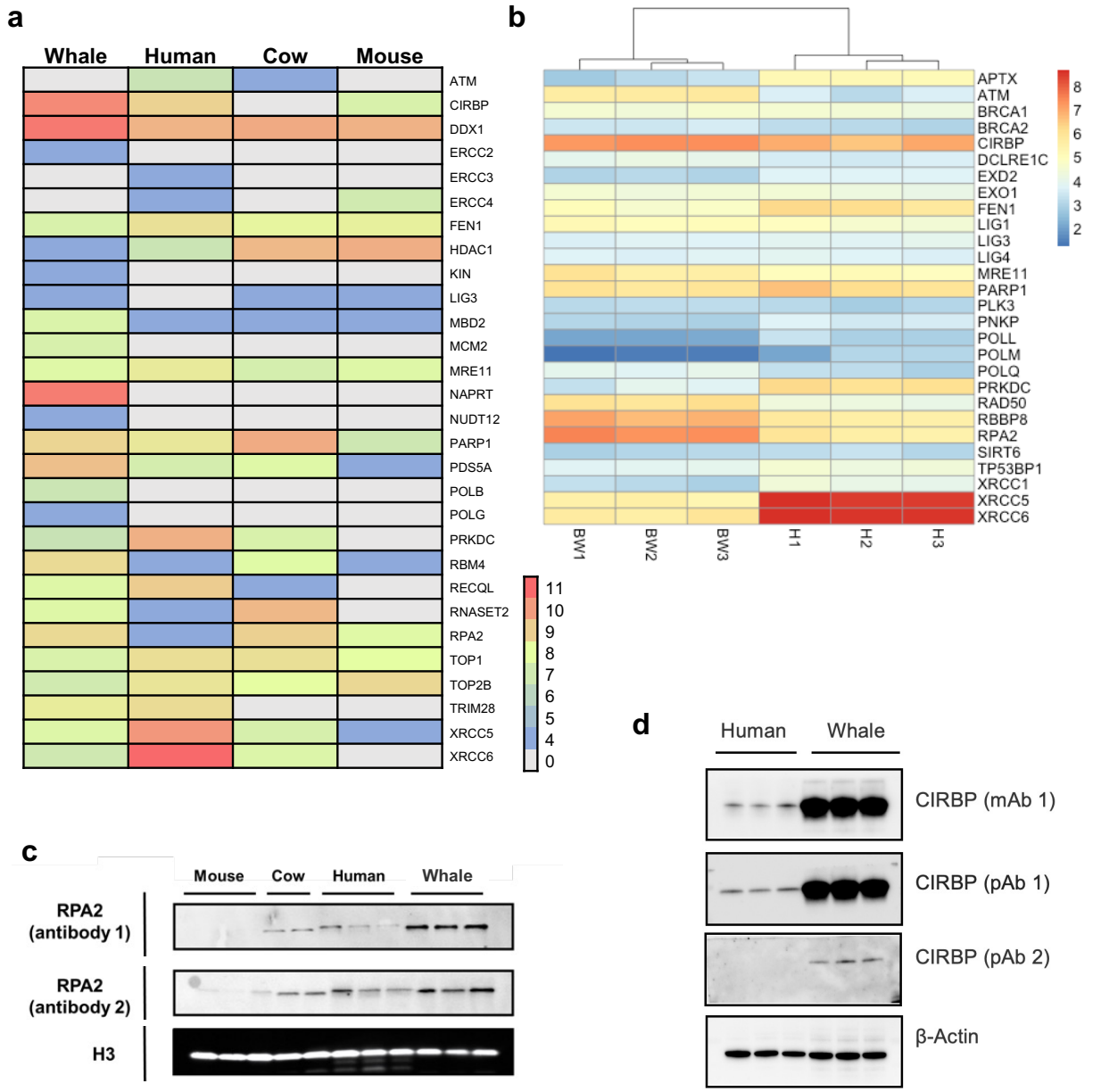

Extended Data Figure 7. Proteomic and transcriptomic quantification of DNA repair proteins. a, Heatmap of LC-MS protein abundance for primary fibroblasts of the indicated species and proteins. Color scale corresponds to $\log_{10}$ ion intensity. **b**, Heatmap of transcript expression from RNA-seq of primary fibroblasts for the indicated species and transcripts. BW, bowhead whale; H, human. Numbers represent different cell lines. Color scale corresponds to normalized transcript abundance as described in Methods. **c**, Western blot of RPA2 in cultured skin fibroblasts, using 2 different monoclonal primary antibodies targeting conserved epitopes and normalized to histone H3. Each lane is a primary fibroblast line from a different adult individual. Fluorescent secondary antibodies were used to increase linear dynamic range for higher quantitative accuracy. **d**, Western blot for CIRBP with 3 different antibodies in 3 fibroblast lines per species. mAb, monoclonal antibody; pAb, polyclonal antibody.

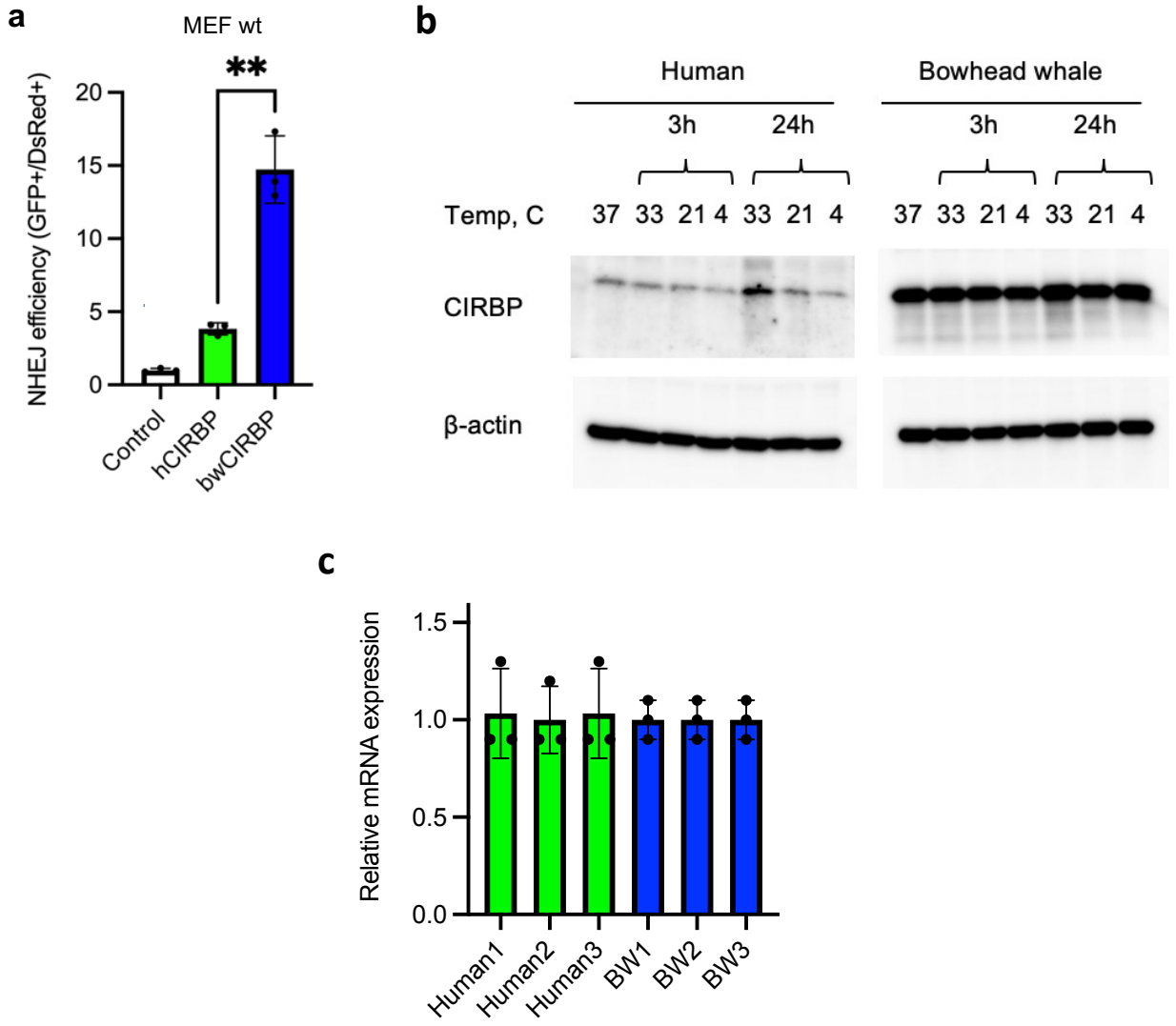

Extended Data Figure 8. Bowhead whale CIRBP stimulates NHEJ in MEFs and effect of temperature on CIRBP expression. a, Effect of bwCIRBP expression on NHEJ in MEFs. CIRBP was expressed in mouse embryonic fibroblasts containing chromosomally integrated NHEJ reporter cassettes. (N=3). MEF, mouse embryonic fibroblasts. **b**, Western blot of CIRBP in human and bowhead whale primary skin fibroblasts at different temperatures. **c**, Relative endogenous CIRBP mRNA expression by qRT-PCR in 3 different human and 3 different bowhead whale cell lines. Error bars represent mean ± SD. ** $p<0.01$. *** $p<0.001$ (two-tailed t-test).

a

```
Human_CIRBP     MASDEGKLFVGGLSFDTNEQSLEQVFSKYGQISEVVVVKDRETQRSRGFGFVTFENIDDA   60
BW_CIRBP        MASDEGKLFVGGLSFDTNEQSLEQVFSKYGQISEVVVVKDRETQRSRGFGFVTFENIDDA   60
                ************************************************************

Human_CIRBP     KDAMMAMNGKSVDGRQIRVDQAGKSSDNRSRGYRGGSAGGRGFFRGGRGRGRGFSRGGGD   120
BW_CIRBP        KDAMMAMNGKSVDGRQIRVDQAGKSSDNRSRGYRGGSAGGRGFFRGGRGRGRGFSRGGGD   120
                ************************************************************

Human_CIRBP     RGYGGNRFESRSGGYGGSRDYYSSRSQSGGYSDRSSGGSYRDSYDSYATHNE   172
BW_CIRBP        RGYGGSRFESRSGGYGGSRDYYSSRSQGGSCGDRSSGGSYRDSYDSYATHNE   172
                *****.**********************.*. .********************
```

b

```
hCIRBP      ATGGCATCAGATGAAGGCAAACTTTTTGTTGGAGGGCTGAGTTTTGACACCAATGAGCAG      60
bwCIRBP     ATGGCATCAGATGAGGGCAAGCTTTTCGTCGGAGGGCTGAGTTTTGACACCAATGAGCAG      60
            ************** ***** ***** ** ******************************

hCIRBP      TCGCTGGAGCAGGTCTTCTCAAAGTACGGACAGATCTCTGAAGTGGTGGTTGTGAAAGAC      120
bwCIRBP     TCACTGGAGCAGGTCTTCTCAAAATATGGACAGATCTCAGAAGTGGTGGTCGTGAAGGAC      120
            ** ******************** ** *********** *********** ***** ***

hCIRBP      AGGGAGACCCAGAGATCTCGGGGATTTGGGTTTGTCACCTTTGAGAACATTGACGACGCT      180
bwCIRBP     AGGGAGACCCAGCGATCGAGGGGCTTTGGGTTTGTCACCTTTGAGAACATCGATGATGCC      180
            ************ ****  **** ************************** ** ** **

hCIRBP      AAGGATGCCATGATGGCCATGAATGGGAAGTCTGTAGATGGACGGCAGATCCGAGTAGAC      240
bwCIRBP     AAGGACGCCATGATGGCCATGAACGGGAAGTCTGTGGATGGGCGGCAGATCCGGGTCGAC      240
            ***** ***************** *********** ***** *********** ** ***

hCIRBP      CAGGCAGGCAAGTCGTCAGACAACCGATCCCGTGGGTACCGTGGTGGCTCTGCCGGGGGC      300
bwCIRBP     CAGGCTGGCAAGTCGTCTGATAACCGATCCCGCGGGTACCGAGGTGGCTCTGCCGGGGGC      300
            ***** *********** ** *********** ******** ******************

hCIRBP      CGGGGCTTCTTCCGTGGGGGCCGAGGACGGGGCCGTGGGTTCTCTAGAGGAGGAGGGGAC      360
bwCIRBP     CGGGGCTTTTTCCGCGGGGGCCGAGGCCGGGGCCGTGGGTTCTCCAGAGGAGGAGGGGAC      360
            ******** ***** *********** ***************** ***************

hCIRBP      CGAGGCTATGGGGGGAACCGGTTCGAGTCCAGGAGTGGGGGCTACGGAGGCTCCAGAGAC      420
bwCIRBP     CGCGGCTACGGGGGGAGCCGGTTCGAGTCCAGGAGTGGGGGCTATGGAGGCTCCAGAGAC      420
            ** ***** ******* *************************** ***************

hCIRBP      TACTATAGCAGCCGGAGTCAGAGTGGTGGCTACAGTGACCGGAGCTCGGGCGGGTCCTAC      480
bwCIRBP     TACTACAGCAGCCGGAGTCAGGGTGGCAGCTGCGGTGATCGAAGCTCGGGCGGGTCCTAC      480
            ***** *************** ****  *** * **** ** ******************

hCIRBP      AGAGACAGTTATGACAGTTACGCTACACACAACGAGTAA    519
bwCIRBP     AGAGACAGCTACGACAGTTACGCTACACACAACGAGTAA    519
            ******** ** ****************************
```

c

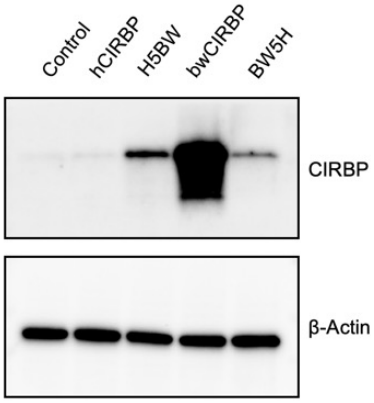

d

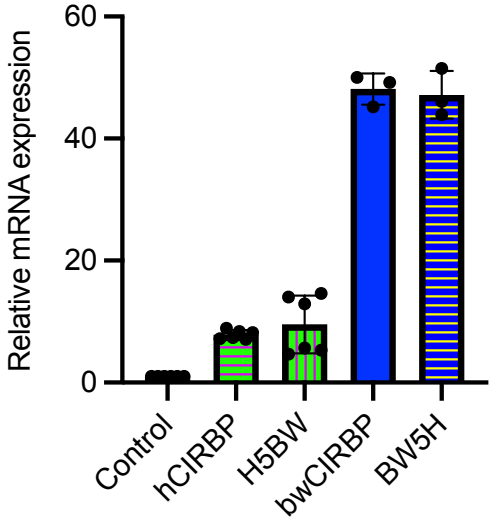

e

CDS variant	CAI
hCIRBP	0.811
bwCIRBP	0.845
H5BW	0.809
BW5H	0.848

Extended Data Figure 9. Effect of CIRBP mutations on mRNA and protein expression. a, Human and whale CIRBP differ by only 5 amino acids. Alignment of bowhead whale and human CIRBP amino acid sequences (Clustal Omega). **b**, Alignment of bowhead whale and human CIRBP coding sequences (Clustal Omega). **c**, Western blot of bwCIRBP, hCIRBP, and reciprocal amino acid mutants overexpressed in human cells. **d**, Total CIRBP mRNA levels in human cells analyzed by qRT-PCR 24h after transfection of plasmids containing either wild type (hCIRBP, bwCIRBP) or mutants encoding hCIRBP with 5 amino acids mutated to whale sequence (H5BW) or bwCIRBP with 5 amino acids from human sequence (BW5H). β-Actin was used for data normalization. Units shown on the graph are relative to human basal endogenous CIRBP mRNA abundance (n=3). **e**, Calculated codon adaptation index (CAI)[53] for CIRBP coding sequence variants. Error bars are mean ± SD.